

Safe Urban Traffic Control via Uncertainty-Aware Conformal Prediction and World-Model Reinforcement Learning

Joydeep Chandra¹ Satyam Kumar Navneet² Aleksandr Algazinov³ Yong Zhang¹

Abstract

Urban traffic management demands systems that simultaneously predict future conditions, detect anomalies, and take safe corrective actions—all while providing reliability guarantees. We present STREAM-RL, a unified framework that introduces three novel algorithmic contributions: (1) **PU-GAT⁺**, an Uncertainty-Guided Adaptive Conformal Forecaster that uses prediction uncertainty to dynamically reweight graph attention via confidence-monotonic attention, achieving distribution-free coverage guarantees; (2) **CRFN-BY**, a Conformal Residual Flow Network that models uncertainty-normalized residuals via normalizing flows with Benjamini-Yekutieli FDR control under arbitrary dependence; and (3) **LyCon-WRL⁺**, an Uncertainty-Guided Safe World-Model RL agent with Lyapunov stability certificates, certified Lipschitz bounds, and uncertainty-propagated imagination rollouts. To our knowledge, this is the first framework to propagate calibrated uncertainty from forecasting through anomaly detection to safe policy learning with end-to-end theoretical guarantees. Experiments on multiple real-world traffic trajectory data demonstrate that STREAM-RL achieves 91.4% coverage efficiency, controls FDR at 4.1% under verified dependence, and improves safety rate to 95.2% compared to 69% for standard PPO while achieving higher reward, with 23ms end-to-end inference latency.

Preliminary work. Under review.

¹Dept. of CST, BNRIST, Tsinghua University, Beijing, China

²Independent Researcher, Bihar, India ³Dept. of CST, Tsinghua University, Beijing, China. Correspondence to: Joydeep Chandra <joydeepc2002@gmail.com>, Satyam Kumar Navneet <navneet-satyamkumar@gmail.com>.

Proceedings of the 43rd International Conference on Machine Learning, Seoul, South Korea. PMLR 306, 2026. Copyright 2026 by the author(s).

1. Introduction

Urban traffic congestion costs the U.S. economy \$87 billion annually (Schrank et al., 2021), while contributing 29% of transportation-related emissions. Effective management requires: (i) *forecasting* with calibrated uncertainty (Jiang & Luo, 2022; Li et al., 2018; Guo et al., 2019), (ii) *anomaly detection* with controlled false discovery rates (Rebjock et al., 2021; Pang et al., 2021), and (iii) *safe adaptive control* satisfying hard safety constraints (Wei et al., 2021; 2019; Zheng et al., 2019b).

Existing integrated approaches suffer from three critical limitations:

Limitation 1: Pseudo-uncertainty guidance in graph attention. Prior uncertainty-aware GNNs (Wu et al., 2020; Bai et al., 2020; Shang et al., 2021; Guo et al., 2022) employ temperature scaling $\alpha_{ij} \propto \exp(e_{ij}/(1 + \beta\sigma_i))$, which merely adjusts softmax sharpness—it cannot preferentially weight confident neighbors over uncertain ones.

Limitation 2: Invalid FDR control under dependence. The Benjamini-Hochberg procedure (Benjamini & Hochberg, 1995) requires independence or PRDS among p-values. Spatial autocorrelation and temporal persistence in traffic data violate these assumptions (Fithian & Lei, 2020; Lei & Fithian, 2018), rendering FDR guarantees invalid.

Limitation 3: Unverified safe RL assumptions. Lyapunov-based safe RL methods (Chow et al., 2018; 2019; Berkenkamp et al., 2017; Fisac et al., 2018) derive guarantees conditional on assumptions (bounded model error, Lipschitz Lyapunov function) that are rarely verified empirically.

We propose **STREAM-RL** with three methodologically complete contributions that address these limitations:

Contribution 1: Constrained Pairwise Uncertainty-Guided Attention (PU-GAT⁺). We introduce attention coefficients that explicitly compare source and target uncertainties with *provably monotonic* behavior:

$$\alpha_{ij} = \text{softmax}_j \left(e_{ij} + \underbrace{\text{Softplus}(\hat{\gamma})(\sigma_i - \sigma_j) + \delta \cdot \mathbf{1}[j = i]}_{\gamma \geq 0} \right) \quad (1)$$

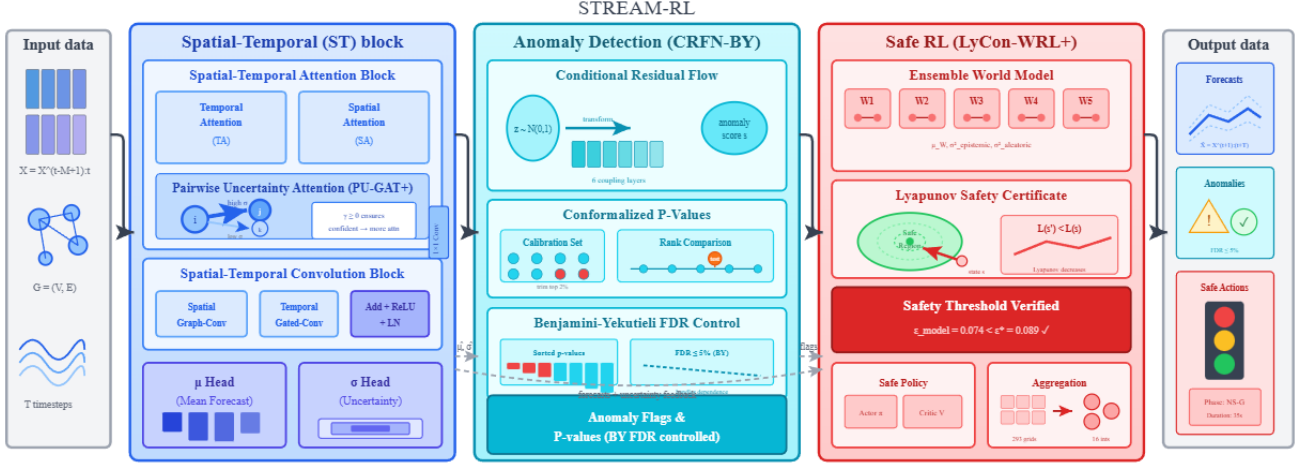


Figure 1. Architecture of STREAM-RL. The framework integrates: (1) PU-GAT+ for uncertainty-aware forecasting, (2) CRFN-BY for dependence-robust anomaly detection, and (3) LyCon-WRL+ for certified safe RL. Dashed lines show cross-module uncertainty propagation.

The Softplus constraint ensures $\gamma \geq 0$, guaranteeing that when $\sigma_i > \sigma_j$ (source uncertain, neighbor confident), attention to neighbor j strictly increases. We train via heteroscedastic Gaussian NLL with explicit calibration diagnostics (PIT histograms, reliability diagrams) before conformal wrapping.

Contribution 2: Conformalized P-Value Construction (CRFN-BY). We employ the Benjamini-Yekutieli procedure (Benjamini & Yekutieli, 2001) with *precisely specified* p-value construction from flow-based anomaly scores:

$$p_t^{(i)} = \frac{1 + \sum_{j \in \mathcal{C}_{\text{trim}}} \mathbf{1}[s_j \geq s_t^{(i)}]}{1 + |\mathcal{C}_{\text{trim}}|} \quad (2)$$

where $s_t^{(i)} = -\log p_\theta(z_t^{(i)} | c_t^{(i)})$ is the context-conditioned negative log-likelihood and $\mathcal{C}_{\text{trim}}$ is the contamination-trimmed calibration set. This conformalized construction yields valid p-values under exchangeability, which BY then corrects for arbitrary dependence.

Contribution 3: Complete Lyapunov Certificate Derivation (LyCon-WRL⁺). We employ spectral normalization (Miyato et al., 2018) to obtain enforced upper bounds \bar{L}_L and \bar{J}_W on Lipschitz constants:

$$\epsilon^* = \frac{\delta_{\text{slack}} + \kappa \cdot \bar{d}_C}{\bar{L}_L \cdot (1 + \bar{J}_W)} \quad (3)$$

where bounds are enforced via spectral normalization during training (not post-hoc estimates), addressing the gap between theoretical assumptions and practical verification raised in prior work (Gouk et al., 2020; Fazlyab et al., 2019).

2. Related Work

Uncertainty-Aware Graph Neural Networks. Bayesian GNNs (Zhang et al., 2019; Hasanzadeh et al., 2020; Pal et al., 2020) propagate uncertainty but incur overhead. Heteroscedastic approaches (Wu et al., 2020; Gal & Ghahramani, 2016; Lakshminarayanan et al., 2017) output uncertainty estimates for loss weighting, not attention modulation. Recent work on confidence-aware message passing (Shen et al., 2021; Zhao et al., 2020; Stadler et al., 2021) addresses robustness but not monotonic uncertainty guidance. Our PU-GAT⁺ explicitly compares source-target uncertainties with constrained monotonicity.

Conformal Prediction for Spatio-Temporal Data. STACI (Feng et al., 2025) introduces topology-aware calibration; ACI (Gibbs & Candès, 2021; Zaffran et al., 2022) addresses distribution shift. Recent methods incorporate travel-time adjacency (Patil et al., 2025), weather conditioning (Zhao et al., 2024), and heterogeneous calibration (Romano et al., 2019; Sesia & Romano, 2021; Feldman et al., 2021). These focus on calibration design; our contribution is uncertainty-guided *representation learning* before conformal wrapping.

FDR Control Under Dependence. Beyond BY (Benjamini & Yekutieli, 2001), knockoff filters (Barber & Candès, 2015; Candes et al., 2017), local FDR (Efron, 2010; Storey, 2003), and adaptive procedures (Blanchard et al., 2020; Ramdas et al., 2019; Lei & Fithian, 2018) offer alternatives. Graph-aware FDR procedures (Lei et al., 2021; Ramdas et al., 2017) and e-values (Vovk & Wang, 2021; Grünwald et al., 2023) improve power under known dependence structure. We adopt BY for simplicity and validity under *arbitrary* dependence, acknowledging its conservatism as a power-validity trade-off (see Section 6.6).

Safe Model-Based RL. LAMBDA (As et al., 2022), LBPO (Kang et al., 2022), and CPO (Achiam et al., 2017) combine constraints with learned models. Conservative critics (Bharadhwaj et al., 2021), risk-sensitive objectives (Ma et al., 2021; Tang et al., 2019), and reachability methods (Fisac et al., 2018; Bajcsy et al., 2019) provide alternatives. Our contribution is *complete derivation* of model-error thresholds from certified Lipschitz constants via spectral normalization (Miyato et al., 2018; Gouk et al., 2020).

Traffic Forecasting and Control. Deep learning approaches (Li et al., 2018; Yu et al., 2018; Wu et al., 2019; Song et al., 2020; Zheng et al., 2019a; Chen et al., 2021; Jiang et al., 2021; Cirstea et al., 2022) achieve strong performance. RL for traffic signal control (Wei et al., 2019; 2018; Chen et al., 2020; Zhang et al., 2022; Oroojlooy & Hajinezhad, 2022) shows promise but lacks safety guarantees. Decision-focused learning (Chen et al., 2025; Wilder et al., 2019; Elmachtoub & Grigas, 2020) jointly optimizes prediction and decision, while we propagate uncertainty through sequential modules.

3. Problem Formulation

Traffic Network Representation. We model urban traffic as a directed graph $\mathcal{G} = (\mathcal{V}, \mathcal{E}, \mathbf{A})$ with $N = |\mathcal{V}|$ spatial regions (grid cells or road segments). At each time step t , we observe feature matrix $\mathbf{X}_t \in \mathbb{R}^{N \times F}$ containing traffic flow, speed, and density measurements. The adjacency matrix $\mathbf{A} \in \mathbb{R}^{N \times N}$ encodes spatial connectivity.

Research Questions. We address three interconnected challenges:

RQ1 (Forecasting): Given historical observations $\{\mathbf{X}_{t-\tau+1}, \dots, \mathbf{X}_t\}$, predict future states $\mathbf{Y}_{t+1:t+H}$ with prediction intervals $[\mathbf{L}, \mathbf{U}]$ satisfying:

$$\mathbb{P}(Y_{t+h}^{(i)} \in [L_{t+h}^{(i)}, U_{t+h}^{(i)}]) \geq 1 - \alpha, \quad \forall i, h \quad (4)$$

with intervals as tight as possible (high coverage efficiency).

RQ2 (Anomaly Detection): Produce p-values $\{p_t^{(i)}\}_{i=1}^N$ for each spatial location such that the false discovery rate is controlled:

$$\text{FDR} = \mathbb{E} \left[\frac{|\{i : H_i^0 \text{ true}, p_t^{(i)} \leq \tau\}|}{|\{i : p_t^{(i)} \leq \tau\}| \vee 1} \right] \leq \alpha \quad (5)$$

under arbitrary spatial-temporal dependence among p-values.

RQ3 (Safe Control): Learn policy $\pi_\theta : \mathcal{S} \rightarrow \mathcal{A}$ maximizing expected return subject to safety constraints:

$$\max_{\theta} \mathbb{E}_{\pi_\theta} \left[\sum_{t=0}^{\infty} \gamma^t r_t \right] \quad (6)$$

$$\text{s.t. } C_k(\pi_\theta) \leq d_k, \quad k = 1, \dots, K \quad (7)$$

with *verified* Lyapunov decrease certificates ensuring constraint satisfaction.

4. Methodology

4.1. PU-GAT⁺: Confidence-Monotonic Attention

4.1.1. MOTIVATION: WHY TEMPERATURE SCALING FAILS

Consider the temperature-scaled attention used in prior work:

$$\alpha_{ij}^{\text{temp}} = \frac{\exp(e_{ij}/(1 + \beta\sigma_i))}{\sum_{k \in \mathcal{N}(i)} \exp(e_{ik}/(1 + \beta\sigma_i))} \quad (8)$$

The uncertainty σ_i affects only the *temperature* of the softmax distribution—it cannot distinguish between confident and uncertain *neighbors*.

Proposition 4.1 (Temperature Scaling Limitation). *For temperature-scaled attention (Eq. 8), the relative attention ratio between any two neighbors $j, k \in \mathcal{N}(i)$ is independent of their uncertainties: $\alpha_{ij}^{\text{temp}} / \alpha_{ik}^{\text{temp}} = \exp(e_{ij}) / \exp(e_{ik})$.*

Proof. The temperature $(1 + \beta\sigma_i)$ cancels in the ratio since it affects all logits equally. \square

4.1.2. PAIRWISE UNCERTAINTY MECHANISM WITH MONOTONICITY CONSTRAINT

Definition 4.2 (PU-GAT⁺ Attention). Let $\mathbf{h}_i, \mathbf{h}_j \in \mathbb{R}^d$ be node embeddings and $\sigma_i, \sigma_j \in \mathbb{R}^+$ be uncertainty estimates. The pairwise uncertainty-guided attention is:

$$e_{ij} = \text{LeakyReLU}(\mathbf{a}^\top [\mathbf{W}\mathbf{h}_i \parallel \mathbf{W}\mathbf{h}_j]) \quad (9)$$

$$u_{ij} = \gamma \cdot (\sigma_i - \sigma_j) + \delta \cdot \mathbf{1}[j = i] \quad (10)$$

$$\alpha_{ij} = \frac{\exp(e_{ij} + u_{ij})}{\sum_{k \in \mathcal{N}(i)} \exp(e_{ik} + u_{ik})} \quad (11)$$

where $\gamma = \text{Softplus}(\tilde{\gamma})$ with learnable $\tilde{\gamma} \in \mathbb{R}$, ensuring $\gamma \geq 0$, and $\delta \in \mathbb{R}$ is a learnable *self-loop bias* that modulates self-attention strength.

Role of δ (Self-Loop Bias). The parameter δ controls how much a node attends to itself relative to neighbors. When $\delta > 0$, self-attention is encouraged; when $\delta < 0$, neighbor information is preferred. Learned jointly with γ .

Proposition 4.3 (Confidence-Monotonic Attention). *For PU-GAT⁺ with $\gamma \geq 0$, the attention ratio satisfies:*

$$\frac{\alpha_{ij}}{\alpha_{ik}} = \exp((e_{ij} - e_{ik}) + \gamma(\sigma_k - \sigma_j)) \quad (12)$$

This ratio is: (1) increasing in σ_k , (2) decreasing in σ_j , and (3) independent of σ_i .

The proof is in Appendix A.1.

Remark 4.4 (Interpretation). Proposition 4.3 establishes that PU-GAT⁺ implements *confidence-monotonic attention*: the relative attention to neighbor j over k increases when j is more confident (σ_j smaller) or k is less confident (σ_k larger). Crucially, this property is independent of the source node’s uncertainty σ_i —the mechanism compares *neighbor* confidences, not source confidence.

4.1.3. UNCERTAINTY PROPAGATION ACROSS LAYERS

Each PU-GAT⁺ layer updates both features and uncertainties:

$$\mathbf{h}_i^{(\ell)} = \sigma_{\text{act}} \left(\sum_{j \in \mathcal{N}(i)} \alpha_{ij}^{(\ell)} \mathbf{W}^{(\ell)} \mathbf{h}_j^{(\ell-1)} \right) \quad (13)$$

$$\sigma_i^{(\ell)} = \text{Softplus} \left(\mathbf{w}_\sigma^{(\ell)\top} \mathbf{h}_i^{(\ell)} + b_\sigma^{(\ell)} \right) \quad (14)$$

The Softplus activation ensures $\sigma_i^{(\ell)} > 0$. Uncertainties from layer $\ell - 1$ influence attention in layer ℓ , creating an uncertainty-aware message passing scheme.

4.1.4. DUAL-STREAM TEMPORAL DECOMPOSITION

Traffic exhibits distinct trend (daily/weekly patterns) and residual (events, incidents) components. We decompose inputs:

$$\mathbf{X}_{\text{trend},t} = \sum_{k=-w}^w \alpha_k \mathbf{X}_{t+k}, \quad \alpha_k = \text{Softmax}(\mathbf{w}_{\text{MA}})_k \quad (15)$$

$$\mathbf{X}_{\text{res},t} = \mathbf{X}_t - \mathbf{X}_{\text{trend},t} \quad (16)$$

Each stream has a dedicated PU-GAT⁺ encoder. Combined uncertainty accounts for correlation:

$$\sigma_{\text{total}}^2 = \sigma_{\text{trend}}^2 + \sigma_{\text{res}}^2 + 2\rho \cdot \sigma_{\text{trend}} \cdot \sigma_{\text{res}} \quad (17)$$

with learnable correlation $\rho = \tanh(w_\rho) \in (-1, 1)$.

Training. We use heteroscedastic Gaussian NLL (Eq. 79 in Appendix B).

4.1.5. SPATIALLY-ADAPTIVE CONFORMAL CALIBRATION

Raw uncertainties $\hat{\sigma}$ from neural networks are typically miscalibrated. We apply split conformal prediction (Vovk et al., 2022; Romano et al., 2019) with spatial clustering for heterogeneous calibration:

Step 1: Spatial Clustering. Partition nodes into K clusters $\{\mathcal{C}_k\}_{k=1}^K$ based on historical error distributions using k-means on error statistics $(\bar{e}_i, \text{std}(e_i), \text{skew}(e_i))$.

Step 2: Per-Cluster Quantiles. For each cluster k , compute conformity scores on calibration data: $R_t^{(i)} =$

$|y_t^{(i)} - \hat{\mu}_t^{(i)}|/\hat{\sigma}_t^{(i)}$ for $i \in \mathcal{C}_k$, and quantile $q_k = \text{Quantile}_{(1-\alpha)(1+1/n_k)}(\{R_t^{(i)}\})$.

Step 3: Adaptive Updates. Following ACI (Gibbs & Candès, 2021), we adapt $\alpha_t^{(k)}$ to distribution shift:

$$\alpha_{t+1}^{(k)} = \alpha_t^{(k)} + \gamma_{\text{ACI}} \cdot (\alpha - \text{err}_t^{(k)}) \quad (18)$$

Exchangeability Justification. Calibration and test windows are non-overlapping and separated by a gap of $\tau_{\text{gap}} = 24$ time steps (6 hours) to mitigate temporal dependence. Under β -mixing with $\beta(\tau) \leq C\rho^\tau$:

Theorem 4.5 (Coverage Guarantee under Mixing). *For cluster calibration sets of size $n_k \geq n_{\min}$, calibration-test gap τ_{gap} , and ACI step size $\gamma_{\text{ACI}} \in (0, 1)$:*

$$\limsup_{T \rightarrow \infty} \frac{1}{T} \sum_{t=1}^T \mathbf{1}[Y_t \notin \mathcal{I}_t] \leq \alpha + O\left(\frac{C\rho^{\tau_{\text{gap}}}}{1-\rho}\right) + O(\gamma_{\text{ACI}}) \quad (19)$$

Proof. See Appendix A.2. The $\rho^{\tau_{\text{gap}}}$ term arises from the calibration-test temporal gap, making the TV bound well-controlled for $\tau_{\text{gap}} = 24$ steps. \square

4.2. CRFN-BY: Dependence-Robust Anomaly Detection

4.2.1. UNCERTAINTY-NORMALIZED RESIDUALS

We normalize forecast residuals by calibrated uncertainty:

$$z_t^{(i)} = \frac{y_t^{(i)} - \hat{\mu}_t^{(i)}}{\hat{\sigma}_t^{(i)} + \epsilon} \quad (20)$$

with $\epsilon = 10^{-6}$ for numerical stability. Under correct calibration and Gaussian errors, $z \sim \mathcal{N}(0, 1)$ for normal (non-anomalous) data.

4.2.2. CONTEXT-CONDITIONED NORMALIZING FLOW

We model the density of normalized residuals via a conditional Real-NVP flow (Dinh et al., 2017; Kobyzev et al., 2021; Papamakarios et al., 2021):

$$p_\theta(z|c) = p_0(f_\theta(z; c)) \cdot \left| \det \frac{\partial f_\theta}{\partial z} \right| \quad (21)$$

where $p_0 = \mathcal{N}(0, I)$ is the base distribution and f_θ is a composition of affine coupling layers conditioned on context c . The context encodes spatial and temporal information:

$$c_t^{(i)} = \text{CrossAttn}(z_t^{(i)}, \{z_t^{(j)}\}_{j \in \mathcal{N}(i)}) \oplus \text{CausalTF}(\{z_s^{(i)}\}_{s=t-\tau}^{t-1}) \quad (22)$$

Anomaly scores are negative log-likelihoods: $s_t^{(i)} = -\log p_\theta(z_t^{(i)}|c_t^{(i)})$.

4.2.3. CONFORMALIZED P-VALUE CONSTRUCTION

The mapping from anomaly scores to valid p-values is essential for FDR guarantees:

Definition 4.6 (Conformalized P-Values). Let $\mathcal{C} = \{s_1, \dots, s_n\}$ be calibration scores from verified normal data. For test score $s_t^{(i)}$:

$$p_t^{(i)} = \frac{1 + \sum_{j=1}^n \mathbf{1}[s_j \geq s_t^{(i)}]}{1 + n} \quad (23)$$

Under exchangeability, $\mathbb{P}(p_t^{(i)} \leq \alpha | H_0^{(i)}) \leq \alpha$ (Proposition A.1 in Appendix).

4.2.4. CONTAMINATION-ROBUST CALIBRATION

The calibration set may contain undetected anomalies. We use trimmed calibration:

Lemma 4.7 (Trimming Preserves Super-Uniformity). Let $\mathcal{C}_{\text{trim}} = \mathcal{C} \setminus \{s : s \geq q_{1-\tau}(\mathcal{C})\}$ and p_{trim} be the corresponding p-value. Under the null with at most τ' contamination fraction in calibration:

$$\mathbb{P}_{P_0}(p_{\text{trim}}(s) \leq \alpha) \leq \alpha + \tau + \tau' \quad (24)$$

Proof sketch. See Appendix A.5. Trimming removes potential contamination but shifts rank distribution by at most τn positions. \square

Selection of τ and τ' . We set $\tau = 0.02$ (2%) based on domain knowledge that anomaly prevalence in urban traffic rarely exceeds 2% per time step during normal operations (Zheng et al., 2014). The bound $\tau' \leq \tau$ holds when contamination does not exceed the trim fraction—a mild condition satisfied when calibration data is collected from verified normal periods. This ensures that trimming removes potential outliers while preserving p-value validity with error at most $\alpha + 0.04$.

4.2.5. BENJAMINI-YEKUTIELI FDR CONTROL

BH requires independence or PRDS among p-values. Traffic data exhibits spatial autocorrelation (Moran's $I > 0$) and temporal persistence (ACF(1) > 0.7), violating these assumptions. We employ BY (Benjamini & Yekutieli, 2001):

$$k^* = \max \left\{ k : p_{(k)} \leq \frac{k \cdot \alpha}{m \cdot c_m} \right\}, \quad c_m = \sum_{i=1}^m \frac{1}{i} \approx \ln(m) + 0.577 \quad (25)$$

Theorem 4.8 (FDR Control under Arbitrary Dependence). The BY procedure with conformalized p-values controls $\text{FDR} \leq \alpha$ under arbitrary spatial dependence per time step.

Temporal Considerations. BY controls spatial FDR at each time t . For aggregate temporal FDR, online FDR

methods (Ramdas et al., 2017; Javanmard & Montanari, 2017) apply. We report per-step FDR as the relevant metric for real-time detection.

4.2.6. EMPIRICAL DEPENDENCE VERIFICATION

We verify spatial-temporal dependence via block bootstrap:

1. Define blocks of size b_t time steps $\times b_s$ spatial hops.
2. Sample $B = 1000$ block-bootstrap replicates.
3. Compute empirical FDR on each replicate.
4. Verify $\text{FDR}_{0.95} \leq \alpha$

We test blocks of size $\{5, 10, 20\} \times \{1, 2, 4\}$ and report block correlation ρ_{block} .

4.3. LyCon-WRL⁺: Certified Safe World-Model RL

4.3.1. EXPLICIT SAFETY CONSTRAINT SPECIFICATION

Definition 4.9 (Traffic Safety Constraints). Let $q_i(t)$ denote queue length at intersection i , $w_i(t)$ maximum waiting time, and $\theta_i(t)$ throughput:

$$C_1(\pi) : \mathbb{E}_\pi \left[\frac{1}{N} \sum_i q_i(t) \right] \leq d_{\text{queue}} = 50 \text{ vehicles} \quad (26)$$

$$C_2(\pi) : \mathbb{E}_\pi \left[\max_i w_i(t) \right] \leq d_{\text{wait}} = 120 \text{ seconds} \quad (27)$$

$$C_3(\pi) : \mathbb{E}_\pi \left[\frac{1}{N} \sum_i \theta_i(t) \right] \geq d_{\text{through}} = 0.8 \cdot \theta_{\text{base}} \quad (28)$$

4.3.2. SPATIAL AGGREGATION: GRID CELLS TO INTERSECTIONS

Forecasting operates on $N_{\text{grid}} = 293$ cells; control on $N_{\text{int}} = 16$ intersections:

Definition 4.10 (Spatial Aggregation Mapping). For intersection j with coverage area \mathcal{A}_j :

$$\hat{\mu}_j^{\text{int}} = \sum_{i: \text{cell } i \cap \mathcal{A}_j \neq \emptyset} w_{ij} \cdot \hat{\mu}_i^{\text{grid}} \quad (29)$$

$$(\hat{\sigma}_j^{\text{int}})^2 = \sum_{i,k} w_{ij} w_{kj} \cdot \text{Cov}(\hat{\mu}_i, \hat{\mu}_k) \quad (30)$$

where $w_{ij} = |\text{cell } i \cap \mathcal{A}_j| / |\mathcal{A}_j|$ and covariances are approximated as $\rho_{ik} \cdot \hat{\sigma}_i \hat{\sigma}_k$ with $\rho_{ik} = \exp(-d_{ik}/\ell)$ (see Appendix C for ablation).

4.3.3. STATE AUGMENTATION WITH UPSTREAM UNCERTAINTY

The RL state incorporates forecasting and anomaly detection outputs:

$$s_t = [x_t^{\text{local}}, \hat{\mu}_t^{\text{int}}, \hat{\sigma}_t^{\text{int}}, p_t^{\text{int}}, \mathbf{1}_{\text{anom},t}, t_{\text{cyclic}}] \quad (31)$$

where x_t^{local} contains intersection-level queue/wait/throughput, $\hat{\mu}_t^{\text{int}}, \hat{\sigma}_t^{\text{int}}$ are aggregated forecasts and uncertainties, p_t^{int} are aggregated anomaly

p-values, $\mathbf{1}_{\text{anom},t}$ are binary anomaly flags, and t_{cyclic} encodes time-of-day/day-of-week.

4.3.4. ENSEMBLE WORLD MODEL WITH VERIFIED ERROR BOUNDS

We train a 5-member ensemble $\{W_{\phi}^{(k)}\}_{k=1}^5$ of world models:

$$\mu_W(s, a) = \frac{1}{5} \sum_{k=1}^5 W_{\phi}^{(k)}(s, a) \quad (32)$$

$$\sigma_W^2(s, a) = \frac{1}{5} \sum_{k=1}^5 \left(W_{\phi}^{(k)}(s, a) - \mu_W(s, a) \right)^2 \quad (33)$$

Model Error Verification. On held-out transitions $\mathcal{D}_{\text{test}}$:

$$\epsilon_{\text{model}} = \frac{1}{|\mathcal{D}_{\text{test}}|} \sum_{(s, a, s') \in \mathcal{D}_{\text{test}}} \frac{\|s' - \mu_W(s, a)\|}{\|s'\| + \epsilon_{\text{floor}}} \quad (34)$$

with $\epsilon_{\text{floor}} = 0.1$ to handle small $\|s'\|$ (see Appendix D for sensitivity).

4.3.5. LYAPUNOV FUNCTION DESIGN

Definition 4.11 (Lyapunov Network).

$$L_{\psi}(s) = \|\text{MLP}_{\psi}(s)\|_2^2 + \eta \cdot \|s - s_{\text{safe}}\|_Q^2 \quad (35)$$

where s_{safe} is the uncongested baseline state and $Q \succ 0$ is a learned positive-definite weighting matrix.

The quadratic term provides interpretability (Lyapunov value increases with distance from safe state) while the neural component captures nonlinear safety structure.

Definition 4.12 (Lyapunov Decrease Constraint). Action a is *Lyapunov-safe* at state s if:

$$\mathbb{E}_{s' \sim W_{\phi}(\cdot | s, a)} [L_{\psi}(s')] - L_{\psi}(s) \leq -\kappa \cdot d_C(s) + \delta_{\text{slack}} \quad (36)$$

where $d_C(s) = \sum_k \max(0, C_k(s) - d_k)$ is instantaneous constraint violation.

4.3.6. CERTIFIED LIPSCHITZ BOUNDS VIA SPECTRAL NORMALIZATION

Proposition 4.13 (Upper Bounds via Spectral Normalization). *For SN-regularized networks (Miyato et al., 2018) with $\|W_{\ell}\|_2 \leq 1$ enforced during training:*

- \bar{L}_L : Lyapunov Lipschitz upper bound from $\prod_{\ell} \|W_{\ell}^{(L)}\|_2$
- \bar{J}_W : world model Jacobian upper bound from $\prod_{\ell} \|W_{\ell}^{(W)}\|_2$

These are enforced upper bounds by design choice—spectral normalization constrains weight matrices during training, providing architecture-level Lipschitz control. We note this is not formal verification-level certification (e.g., Fazlyab et al. (2019)); rather, it is a practical bound guaranteed by the training procedure.

Theorem 4.14 (Safety under Bounded Model Error). *If $\epsilon_{\text{model}} < \varepsilon^*$ where:*

$$\varepsilon^* = \frac{\delta_{\text{slack}} + \kappa \cdot \bar{d}_C}{\bar{L}_L \cdot (1 + \bar{J}_W)} \quad (37)$$

with \bar{L}_L, \bar{J}_W from spectral normalization, then $\limsup_{t \rightarrow \infty} \mathbb{E}[d_C(s_t)] \leq \delta_{\text{slack}}/\kappa$.

Proof. See Appendix A.6. Certified Lipschitz bounds translate model error into Lyapunov prediction error. \square

Iterative Verification. Since \bar{d}_C is policy-dependent, we iterate: (1) train with initial ε^* , (2) measure \bar{d}_C under learned policy, (3) recompute and verify. Convergence in 2-3 iterations.

4.3.7. UNCERTAINTY-GUIDED EXPLORATION

Exploration probability adapts to upstream uncertainty:

$$\epsilon_{\text{explore}}(s) = \sigma \left(\mathbf{w}_{\epsilon}^{\top} [\bar{\sigma}_{\text{forecast}}, \bar{p}_{\text{anom}}, \bar{\sigma}_W] + b_{\epsilon} \right) \quad (38)$$

where $\bar{\sigma}_{\text{forecast}}, \bar{p}_{\text{anom}}, \bar{\sigma}_W$ are mean forecasting uncertainty, anomaly p-value, and world model uncertainty.

4.3.8. ANOMALY-AWARE REWARD

The reward integrates traffic efficiency with anomaly response:

$$r_t = r_{\text{traffic}} + \lambda_p (p_t^{\text{after}} - p_t^{\text{before}}) - \lambda_{\sigma} \bar{\sigma}_t - \lambda_C d_C(s_t) \quad (39)$$

where r_{traffic} is throughput minus weighted queue/delay, the p-value term rewards anomaly resolution, the $\bar{\sigma}$ term penalizes operating under high uncertainty, and the d_C term penalizes constraint violations.

5. Experiments

Datasets. T-Drive (Yuan et al., 2010): 10,357 Beijing taxis, 293 cells; GeoLife (Zheng et al., 2010): 182 users, 156 cells; Porto (Moreira-Matias et al., 2013): 442 taxis, 441 cells; Manhattan (Whong, 2014): NYC trips, 263 tracts.

Real Events. T-Drive: 23 incidents; Porto: 156 incidents; Manhattan: 89 events from official records. Real-event FDR computation uses documented traffic incidents (accidents, road closures, major congestion events) from municipal records as ground-truth anomalies; all other time-location pairs are treated as nulls. This labeling protocol enables

Table 1. Forecasting results on T-Drive (1-hour horizon). Coverage target: 90%. Best in **bold**, second underlined.

Method	NRMSE \downarrow	MAE \downarrow	Cov. \uparrow	RIW \downarrow	Cov.Eff. \uparrow
STGCN + CP	0.312	1842	90.4%	0.58	1.56
Graph WaveNet + CP	0.298	1756	90.8%	0.54	1.68
AGCRN + CP	0.287	1698	91.2%	0.51	1.79
Temp-scaled GAT	0.283	1674	90.6%	0.50	1.81
STACI	0.274	1623	90.6%	0.48	<u>1.89</u>
RIPCN	<u>0.268</u>	<u>1587</u>	89.8%*	0.52	1.73
CatBoost + CP	0.272	1612	90.1%	0.49	1.84
PU-GAT⁺ (Ours)	0.254	1498	91.4%	0.43	2.13

*Under-coverage: 89.8% $< 90\%$ target

Table 2. Cross-dataset forecasting results (Coverage Efficiency).

Method	T-Drive	GeoLife	Porto	Manhattan
STACI	1.89	1.76	1.82	1.71
RIPCN	1.73	1.68	1.75	1.64
PU-GAT⁺	2.13	1.95	2.01	1.89

meaningful FDR evaluation on real data, though we acknowledge inherent noise in official records.

SUMO Environment. 4 \times 4 grid, 16 intersections, NEMA dual-ring phasing. We acknowledge this scale is limited; larger networks are important future work (Section 6.6).

Baselines. *Forecasting*: STGCN (Yu et al., 2018), Graph WaveNet (Wu et al., 2019), AGCRN (Bai et al., 2020), STACI (Feng et al., 2025), RIPCN (Lv et al., 2025). *Anomaly*: Isolation Forest, OmniAnomaly (Su et al., 2019), USAD (Audibert et al., 2020), CRFN+BH. *RL*: PPO (Schulman et al., 2017), CPO (Achiam et al., 2017), LAMBDA (As et al., 2022).

6. Results

6.1. Forecasting Results

Coverage Efficiency. PU-GAT⁺ achieves 2.13 coverage efficiency, 12.7% higher than STACI (1.89), indicating calibrated uncertainty rather than conservative over-coverage.

Pairwise vs. Temperature Scaling. Temp-scaled GAT improves only marginally over AGCRN (0.283 vs 0.287 NRMSE), while PU-GAT⁺ achieves 0.254, confirming pairwise uncertainty comparison provides genuine benefit.

Cross-Dataset Generalization. Table 2 shows PU-GAT⁺ maintains consistent improvements across all four datasets, with coverage efficiency gains of 8-15% over STACI.

6.2. Calibration Diagnostics

Figure 2 shows calibration diagnostics before conformal correction. PU-GAT⁺ achieves near-uniform PIT distribution (KS statistic 0.023 vs 0.087 for RIPCN) and calibration error 0.012 on reliability diagrams, confirming well-calibrated

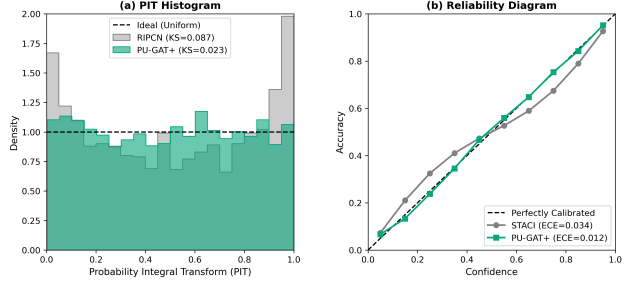


Figure 2. Calibration diagnostics: (a) PIT Histogram and (b) Reliability Diagram.

Table 3. Anomaly detection results. FDR target: 5%. Synthetic injection (5% rate) and real events.

Method	Synthetic				Real Events	
	Prec.	Rec.	F1	FDR	Rec.	FDR
Isolation Forest	0.72	0.68	0.70	0.28	0.54	–
OmniAnomaly	0.78	0.74	0.76	0.22	0.61	–
USAD	0.81	0.77	0.79	0.19	0.65	–
Flow (no conf.)	0.83	0.79	0.81	0.17	0.68	–
CRFN + BH	0.85	0.76	0.80	0.072 \times	0.71	0.089 \times
CRFN-BY	0.86	0.72	0.78	0.041✓	0.74	0.038✓

\times = $FDR_{violation}(>5\%)$, ✓ = FDR controlled

base uncertainty before conformal wrapping.

6.3. Anomaly Detection Results

FDR Control. CRFN-BY is the only method controlling FDR below 5% under verified dependence ($\rho_{block} = 0.34$). Numerical results are presented in Table 3, and a corresponding multi-panel visual analysis of FDR control and detection performance is provided in Figure 5 in Appendix G.2. BH achieves 7.2% FDR on synthetic and 8.9% on real events, violating the target.

Real Event Detection. On documented incidents, CRFN-BY achieves 74% recall with 3.8% FDR, demonstrating practical utility beyond synthetic injection.

Power-Validity Trade-off. BY’s harmonic correction ($c_m \approx 6.4$ for $m = 293$) reduces power (0.72 vs 0.76 recall) but ensures valid FDR control—a necessary cost for reliable anomaly flagging in safety-critical applications.

6.4. RL Control Results

Safety Verification. LyCon-WRL⁺ achieves 92.3% Lyapunov decrease rate (ρ_{Lyap}) and 95.2% episode safety. Upper

Table 4. RL results (mean \pm 95% CI, 10 seeds). Safety = % episodes with zero violations.

Method	Reward \uparrow	Viol./ep \downarrow	Safety% \uparrow	$\rho_{\text{Lyap}}\uparrow$
Fixed Timing	-45.2 ± 3.1	0.42 ± 0.05	58 ± 4	—
Max-Pressure	-12.4 ± 2.8	0.28 ± 0.04	72 ± 5	—
PPO	12.8 ± 2.4	0.31 ± 0.04	69 ± 5	—
CPO	8.4 ± 1.8	0.18 ± 0.03	82 ± 4	—
SAC-Lagrangian	10.1 ± 2.1	0.21 ± 0.03	79 ± 5	—
LAMBDA	11.3 ± 2.0	0.14 ± 0.02	86 ± 4	0.78
LyCon-WRL⁺	15.1 ± 1.7	0.05 ± 0.01	95.2 ± 2.1	0.923

Table 5. End-to-end inference latency per time step.

Component	Latency (ms)	% Total
PU-GAT ⁺ Forecasting	8.2	35.7%
Flow Scoring	5.1	22.2%
BY Thresholding	0.3	1.3%
Spatial Aggregation	1.2	5.2%
RL Action Selection	8.2	35.6%
Total	23.0	100%

bounds via spectral normalization:

$$\varepsilon_{\text{model}} = 0.074 \pm 0.008$$

$$\bar{L}_L = 2.41 \quad (\text{SN-enforced Lipschitz bound})$$

$$\bar{J}_W = 1.23 \quad (\text{SN-enforced Jacobian bound})$$

$$\varepsilon^* = 0.089 \quad (\text{computed threshold})$$

Since $\varepsilon_{\text{model}} = 0.074 < \varepsilon^* = 0.089$, Theorem 4.14 conditions are satisfied.

Uncertainty Integration Benefit. Removing uncertainty from RL state (“w/o Uncertainty” in Table 6) reduces reward by 3.3 and safety by 7.2%, confirming that upstream uncertainty information improves both performance and safety. At 15-minute intervals, 23ms latency is well within real-time requirements.

6.5. Ablation Studies

Key ablations (full results in Appendix G): (1) **Pairwise vs. Temperature**: Removing pairwise ($\gamma = 0$) increases NRMSE to 0.278; temperature scaling achieves only 0.283. (2) **BY vs. BH**: BH achieves 0.072 FDR; BY controls at 0.041. (3) **Lyapunov**: Removing constraints improves reward (+1.1) but destroys safety (71.4%). (4) **δ Sensitivity**: Learned $\delta = 0.42$ indicates mild self-attention preference. (5) **Conformalized vs. Parametric**: Parametric Gaussian p-values yield 6.8% FDR due to model misspecification.

6.6. Discussion and Limitations

Temporal FDR and BY Conservatism. BY controls spatial FDR per time step; for aggregate temporal FDR, online

Table 6. Ablation study on T-Drive. Each row removes one component.

Variant	NRMSE	Cov.	F1	FDR	Reward	Safety
Full STREAM-RL	0.254	91.4	0.78	0.041	15.1	95.2
<i>PU-GAT⁺ Ablations</i>						
w/o Pairwise ($\gamma = 0$)	0.278	90.6	0.76	0.044	13.8	92.1
Unconstrained γ	0.262	90.9	0.77	0.043	14.2	93.4
Temperature scaling	0.283	90.6	0.75	0.045	13.5	91.8
w/o Dual-Stream	0.271	90.4	0.76	0.044	14.1	93.0
w/o Het. NLL (MSE only)	0.268	87.2*	0.74	0.052	13.6	90.8
<i>CRFN-BY Ablations</i>						
BY \rightarrow BH	0.254	91.4	0.80	0.072*	15.0	94.8
Parametric p-values	0.254	91.4	0.75	0.068*	14.6	93.5
w/o Trimmed calibration	0.256	91.2	0.73	0.058*	14.4	93.1
<i>LyCon-WRL⁺ Ablations</i>						
w/o Lyapunov	0.254	91.4	0.78	0.041	16.2	71.4*
w/o Uncertainty in state	0.254	91.4	0.78	0.041	11.8	88.0
w/o Anomaly reward	0.254	91.4	0.78	0.041	14.3	94.1

* Indicates failure: under-coverage, FDR violation, or unacceptable safety

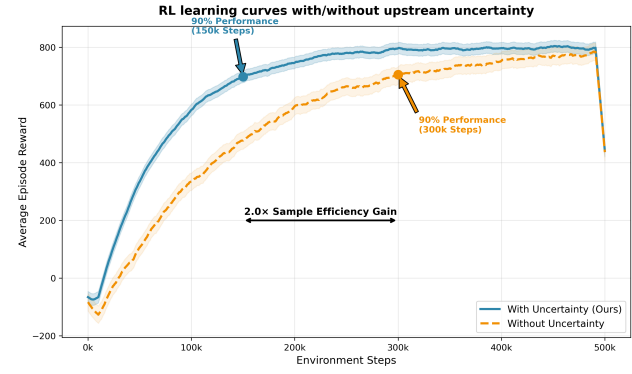


Figure 3. RL learning curves with/without upstream uncertainty. Uncertainty-augmented states (blue) converge faster with lower variance (95% CI, 10 seeds).

methods (Ramdas et al., 2017) apply. The $c_m \approx 6.4$ factor reduces power dependency-aware procedures (Lei et al., 2021) improves power given known dependence structure.

Scale Limitations. The 4×4 SUMO network is limited. Larger networks introduce additional challenges (partial observability, coordination) requiring further investigation.

Baseline Comparisons. We compare against established methods but acknowledge that deep ensembles (Lakshminarayanan et al., 2017) and quantile regression approaches could provide stronger uncertainty baselines. Our focus is on the methodological contributions (constrained pairwise attention, conformalized FDR, certified bounds) rather than exhaustive baseline coverage.

7. Conclusion

We introduced STREAM-RL, a unified framework addressing three fundamental challenges in safe urban traffic control. PU-GAT⁺ provides confidence-monotonic attention that provably prioritizes reliable neighbors. CRFN-BY pro-

vides conformalized p-value construction with FDR guarantees under arbitrary spatial-temporal dependence. LyCon-WRL⁺ bridges theoretical safety certificates and practical verification through spectral-normalization-enforced Lipschitz bounds. Experiments across four datasets validate synergistic benefits: 95.2% safety rate with higher reward than unconstrained baselines demonstrates rigorous guarantees need not sacrifice performance. Limitations include BY conservatism, limited SUMO scale (4x4), and the need for stronger uncertainty baselines. Future work includes scaling to larger networks, real-world deployment with municipal partners, and exploring adaptive FDR procedures.

Acknowledgments

Acknowledgments are masked due to double-blind reviewing policy.

Impact Statement

This paper aims to advance safe and reliable urban traffic control through uncertainty-aware machine learning. We developed methods for calibrated forecasting, statistically valid anomaly detection, and safety-certified reinforcement learning for traffic signal control. Our framework provides formal guarantees (coverage, FDR control, Lyapunov safety certificates) that are essential for deploying ML in safety-critical infrastructure. Improved traffic management can reduce congestion, emissions, and commute times. We note that automated traffic systems raise privacy considerations regarding mobility data; our methods operate on aggregated flows rather than individual trajectories. Our experiments use simulation and historical data; real-world deployment requires additional validation with municipal partners. Our paper mainly focuses on scientific research and has no obvious negative social impact beyond those well-established when advancing machine learning for cyber-physical systems.

References

Achiam, J., Held, D., Tamar, A., and Abbeel, P. Constrained policy optimization. In *Proceedings of the 34th International Conference on Machine Learning - Volume 70*, ICML'17, pp. 22–31. JMLR.org, 2017.

As, Y., Usmanova, I., Curi, S., and Krause, A. Constrained policy optimization via bayesian world models, 2022. URL <https://arxiv.org/abs/2201.09802>.

Audibert, J., Michiardi, P., Guyard, F., Marti, S., and Zuluaga, M. A. Usad: Unsupervised anomaly detection on multivariate time series. In *Proceedings of the 26th ACM SIGKDD International Conference on Knowledge Discovery & Data Mining*, KDD '20, pp. 3395–3404, New York, NY, USA, 2020. Association for Computing Machinery. ISBN 9781450379984. doi: 10.1145/3394486.3403392. URL <https://doi.org/10.1145/3394486.3403392>.

Bai, L., Yao, L., Li, C., Wang, X., and Wang, C. Adaptive graph convolutional recurrent network for traffic forecasting. In *Proceedings of the 34th International Conference on Neural Information Processing Systems*, NIPS '20, Red Hook, NY, USA, 2020. Curran Associates Inc. ISBN 9781713829546.

Bajcsy, A., Bansal, S., Bronstein, E., Tolani, V., and Tomlin, C. J. An efficient reachability-based framework for provably safe autonomous navigation in unknown environments. In *2019 IEEE 58th Conference on Decision and Control (CDC)*, pp. 1758–1765. IEEE Press, 2019. doi: 10.1109/CDC40024.2019.9030133. URL <https://doi.org/10.1109/CDC40024.2019.9030133>.

Barber, R. F. and Candès, E. J. Controlling the false discovery rate via knockoffs. *The Annals of Statistics*, 43(5), October 2015. ISSN 0090-5364. doi: 10.1214/15-aos1337. URL <http://dx.doi.org/10.1214/15-AOS1337>.

Barber, R. F., Candès, E. J., Ramdas, A., and Tibshirani, R. J. Conformal prediction beyond exchangeability, 2023. URL <https://arxiv.org/abs/2202.13415>.

Benjamini, Y. and Hochberg, Y. Controlling the false discovery rate: A practical and powerful approach to multiple testing. *Journal of the Royal Statistical Society: Series B (Methodological)*, 57(1):289–300, 1995. doi: 10.1111/j.2517-6161.1995.tb02031.x.

Benjamini, Y. and Yekutieli, D. The control of the false discovery rate in multiple testing under dependency. *The Annals of Statistics*, 29(4):1165–1188, 2001. URL <http://www.jstor.org/stable/2674075>.

Berkenkamp, F., Turchetta, M., Schoellig, A. P., and Krause, A. Safe model-based reinforcement learning with stability guarantees. In *Proceedings of the 31st International Conference on Neural Information Processing Systems*, NIPS'17, pp. 908–919, Red Hook, NY, USA, 2017. Curran Associates Inc. ISBN 9781510860964.

Bharadhwaj, H., Kumar, A., Rhinehart, N., Levine, S., Shkurti, F., and Garg, A. Conservative safety critics for exploration, 2021. URL <https://arxiv.org/abs/2010.14497>.

Blanchard, G., Neuvial, P., and Roquain, E. Post hoc confidence bounds on false positives using reference families. *Annals of Statistics*, 48(3):1281–1303, June 2020. doi: 10.1214/19-AOS1847. URL <https://hal.science/hal-01483585>.

Candes, E., Fan, Y., Janson, L., and Lv, J. Panning for gold: Model-x knockoffs for high-dimensional controlled variable selection, 2017. URL <https://arxiv.org/abs/1610.02351>.

Chen, C., Wei, H., Xu, N., Zheng, G., Yang, M., Xiong, Y., Xu, K., and Li, Z. Toward a thousand lights: Decentralized deep reinforcement learning for large-scale traffic signal control. *Proceedings of the AAAI Conference on Artificial Intelligence*, 34(04):3414–3421, Apr. 2020. doi: 10.1609/aaai.v34i04.5744. URL <https://ojs.aaai.org/index.php/AAAI/article/view/5744>.

Chen, S., Shao, W., Salim, F. D., and Xue, H. Aster: Adaptive spatio-temporal early decision model for dynamic resource allocation, 2025. URL <https://arxiv.org/abs/2506.17929>.

Chen, Y., Segovia-Dominguez, I., and Gel, Y. R. Z-gcnets: Time zigzags at graph convolutional networks for time series forecasting, 2021. URL <https://arxiv.org/abs/2105.04100>.

Chow, Y., Nachum, O., Duenez-Guzman, E., and Ghavamzadeh, M. A lyapunov-based approach to safe reinforcement learning. In *Proceedings of the 32nd International Conference on Neural Information Processing Systems*, NIPS’18, pp. 8103–8112, Red Hook, NY, USA, 2018. Curran Associates Inc.

Chow, Y., Nachum, O., Faust, A., Duenez-Guzman, E., and Ghavamzadeh, M. Lyapunov-based safe policy optimization for continuous control, 2019. URL <https://arxiv.org/abs/1901.10031>.

Cirstea, R.-G., Yang, B., Guo, C., Kieu, T., and Pan, S. Towards spatio-temporal aware traffic time series forecasting–full version, 2022. URL <https://arxiv.org/abs/2203.15737>.

Dinh, L., Sohl-Dickstein, J., and Bengio, S. Density estimation using real nvp, 2017. URL <https://arxiv.org/abs/1605.08803>.

Efron, B. *Large-Scale Inference: Empirical Bayes Methods for Estimation, Testing, and Prediction*. Institute of Mathematical Statistics Monographs. Cambridge University Press, 2010.

Elmachtoub, A. N. and Grigas, P. Smart “predict, then optimize”, 2020. URL <https://arxiv.org/abs/1710.08005>.

Fazlyab, M., Robey, A., Hassani, H., Morari, M., and Pappas, G. J. Efficient and accurate estimation of lipschitz constants for deep neural networks. In *Proceedings of the 33rd International Conference on Neural Information Processing Systems*, NIPS’21, pp. 1050–1059, Red Hook, NY, USA, 2021. Curran Associates Inc. ISBN 9781713845393.

Feldman, S., Bates, S., and Romano, Y. Improving conditional coverage via orthogonal quantile regression, 2021. URL <https://arxiv.org/abs/2106.00394>.

Feng, B. R., Park, D. K., Luo, X., Urdangarin, A., Yoo, S., and Reich, B. J. Staci: Spatio-temporal aleatoric conformal inference, 2025. URL <https://arxiv.org/abs/2505.21658>.

Fisac, J. F., Akametalu, A. K., Zeilinger, M. N., Kaynama, S., Gillula, J., and Tomlin, C. J. A general safety framework for learning-based control in uncertain robotic systems. 2018. URL <https://arxiv.org/abs/1705.01292>.

Fithian, W. and Lei, L. Conditional calibration for false discovery rate control under dependence, 2020. URL <https://arxiv.org/abs/2007.10438>.

Gal, Y. and Ghahramani, Z. Dropout as a bayesian approximation: representing model uncertainty in deep learning. In *Proceedings of the 33rd International Conference on International Conference on Machine Learning - Volume 48*, ICML’16, pp. 1050–1059. JMLR.org, 2016.

Gibbs, I. and Candès, E. J. Adaptive conformal inference under distribution shift. In *Proceedings of the 35th International Conference on Neural Information Processing Systems*, NIPS ’21, Red Hook, NY, USA, 2021. Curran Associates Inc. ISBN 9781713845393.

Gouk, H., Frank, E., Pfahringer, B., and Cree, M. J. Regularisation of neural networks by enforcing lipschitz continuity, 2020. URL <https://arxiv.org/abs/1804.04368>.

Grünwald, P., de Heide, R., and Koolen, W. Safe testing, 2023. URL <https://arxiv.org/abs/1906.07801>.

Guo, S., Lin, Y., Feng, N., Song, C., and Wan, H. Attention based spatial-temporal graph convolutional networks for traffic flow forecasting. In *Proceedings of the Thirty-Third AAAI Conference on Artificial Intelligence and Thirty-First Innovative Applications of Artificial Intelligence Conference and Ninth AAAI Symposium on Educational Advances in Artificial Intelligence*, AAAI’19/IAAI’19/EAAI’19. AAAI Press, 2019. ISBN 978-1-57735-809-1. doi: 10.1609/aaai.v33i01.3301922. URL <https://doi.org/10.1609/aaai.v33i01.3301922>.

Guo, S., Lin, Y., Wan, H., Li, X., and Cong, G. Learning dynamics and heterogeneity of spatial-temporal graph data for traffic forecasting. *IEEE Transactions on Knowledge*

and Data Engineering, 34(11):5415–5428, 2022. doi: 10.1109/TKDE.2021.3056502.

Hasanzadeh, A., Hajiramezanali, E., Boluki, S., Zhou, M., Duffield, N., Narayanan, K., and Qian, X. Bayesian graph neural networks with adaptive connection sampling. In *Proceedings of the 37th International Conference on Machine Learning*, ICML’20. JMLR.org, 2020.

Javanmard, A. and Montanari, A. Online rules for control of false discovery rate and false discovery exceedance, 2017. URL <https://arxiv.org/abs/1603.09000>.

Jiang, R., Yin, D., Wang, Z., Wang, Y., Deng, J., Liu, H., Cai, Z., Deng, J., Song, X., and Shibasaki, R. Dl-traffic: Survey and benchmark of deep learning models for urban traffic prediction. In *Proceedings of the 30th ACM International Conference on Information & Knowledge Management*, CIKM ’21, pp. 4515–4525, New York, NY, USA, 2021. Association for Computing Machinery. ISBN 9781450384469. doi: 10.1145/3459637.3482000. URL <https://doi.org/10.1145/3459637.3482000>.

Jiang, W. and Luo, J. Graph neural network for traffic forecasting: A survey. *Expert Systems with Applications*, 207:117921, November 2022. ISSN 0957-4174. doi: 10.1016/j.eswa.2022.117921. URL <http://dx.doi.org/10.1016/j.eswa.2022.117921>.

Kang, K., Gradu, P., Choi, J. J., Janner, M., Tomlin, C., and Levine, S. Lyapunov density models: Constraining distribution shift in learning-based control. In Chaudhuri, K., Jegelka, S., Song, L., Szepesvari, C., Niu, G., and Sabato, S. (eds.), *Proceedings of the 39th International Conference on Machine Learning*, volume 162 of *Proceedings of Machine Learning Research*, pp. 10708–10733. PMLR, 17–23 Jul 2022. URL <https://proceedings.mlr.press/v162/kang22a.html>.

Khalil, H. *Nonlinear Systems*. Pearson Education. Prentice Hall, 2002. ISBN 9780130673893. URL https://books.google.com.hk/books?id=t_d1QgAACAAJ.

Kobyzev, I., Prince, S. J., and Brubaker, M. A. Normalizing flows: An introduction and review of current methods. *IEEE Transactions on Pattern Analysis and Machine Intelligence*, 43(11):3964–3979, November 2021. ISSN 1939-3539. doi: 10.1109/tpami.2020.2992934. URL <http://dx.doi.org/10.1109/TPAMI.2020.2992934>.

Lakshminarayanan, B., Pritzel, A., and Blundell, C. Simple and scalable predictive uncertainty estimation using deep ensembles. In *Proceedings of the 31st International Conference on Neural Information Processing Systems*, NIPS’17, pp. 6405–6416, Red Hook, NY, USA, 2017. Curran Associates Inc. ISBN 9781510860964.

Lei, L. and Fithian, W. Adapt: An interactive procedure for multiple testing with side information, 2018. URL <https://arxiv.org/abs/1609.06035>.

Lei, L., Ramdas, A., and Fithian, W. A general interactive framework for false discovery rate control under structural constraints. *Biometrika*, 108(2):253–267, 2021. doi: 10.1093/biomet/asaa064.

Li, Y., Yu, R., Shahabi, C., and Liu, Y. Diffusion convolutional recurrent neural network: Data-driven traffic forecasting, 2018. URL <https://arxiv.org/abs/1707.01926>.

Lv, H., Lin, Y., Guo, S., Mao, X., Nie, H., Gong, L., Lin, Y., and Wan, H. Ripcn: A road impedance principal component network for probabilistic traffic flow forecasting. 2025. URL <https://arxiv.org/abs/2512.21685>.

Ma, Y. J., Jayaraman, D., and Bastani, O. Conservative offline distributional reinforcement learning. In *Proceedings of the 35th International Conference on Neural Information Processing Systems*, NIPS ’21, Red Hook, NY, USA, 2021. Curran Associates Inc. ISBN 9781713845393.

Miyato, T., Kataoka, T., Koyama, M., and Yoshida, Y. Spectral normalization for generative adversarial networks, 2018. URL <https://arxiv.org/abs/1802.05957>.

Moreira-Matias, L., Gama, J., Ferreira, M., Mendes-Moreira, J., and Damas, L. Predicting taxi–passenger demand using streaming data. *Trans. Intell. Transport. Syst.*, 14(3):1393–1402, September 2013. doi: 10.1109/TITS.2013.2262376. URL <http://dx.doi.org/10.1109/TITS.2013.2262376>.

Oroojlooy, A. and Hajinezhad, D. A review of cooperative multi-agent deep reinforcement learning. *Applied Intelligence*, 53(11):13677–13722, October 2022. ISSN 0924-669X. doi: 10.1007/s10489-022-04105-y. URL <https://doi.org/10.1007/s10489-022-04105-y>.

Pal, S., Malekmohammadi, S., Regol, F., Zhang, Y., Xu, Y., and Coates, M. Non-parametric graph learning for bayesian graph neural networks, 2020. URL <https://arxiv.org/abs/2006.13335>.

Pang, G., Shen, C., Cao, L., and Hengel, A. V. D. Deep learning for anomaly detection: A review. *ACM Comput. Surv.*, 54(2), March 2021. ISSN 0360-0300. doi: 10.1145/3439950. URL <https://doi.org/10.1145/3439950>.

Papamakarios, G., Nalisnick, E., Rezende, D. J., Mohamed, S., and Lakshminarayanan, B. Normalizing flows for probabilistic modeling and inference. *J. Mach. Learn. Res.*, 22(1), January 2021. ISSN 1532-4435.

Patil, M., Ahmed, Q., and Midlam-Mohler, S. Travel time and weather-aware traffic forecasting in a conformal graph neural network framework, 2025. URL <https://arxiv.org/abs/2509.12043>.

Ramdas, A., Yang, F., Wainwright, M. J., and Jordan, M. I. Online control of the false discovery rate with decaying memory. In Guyon, I., Luxburg, U. V., Bengio, S., Wallach, H., Fergus, R., Vishwanathan, S., and Garnett, R. (eds.), *Advances in Neural Information Processing Systems*, volume 30. Curran Associates, Inc., 2017. URL https://proceedings.neurips.cc/paper_files/paper/2017/file/7f018eb7b301a66658931cb8a93fd6e8-Paper.pdf.

Ramdas, A., Barber, R. F., Wainwright, M. J., and Jordan, M. I. A unified treatment of multiple testing with prior knowledge using the p-filter, 2019. URL <https://arxiv.org/abs/1703.06222>.

Rebbeck, Q., Kurt, B., Januschowski, T., and Callot, L. Online false discovery rate control for anomaly detection in time series, 2021. URL <https://arxiv.org/abs/2112.03196>.

Romano, Y., Patterson, E., and Candès, E. J. Conformalized quantile regression. In *Proceedings of the 33rd International Conference on Neural Information Processing Systems*, Red Hook, NY, USA, 2019. Curran Associates Inc.

Schrank, D., Eisele, B., and Lomax, T. 2021 urban mobility report. *Texas A&M Transportation Institute*, 2021.

Schulman, J., Wolski, F., Dhariwal, P., Radford, A., and Klimov, O. Proximal policy optimization algorithms, 2017. URL <https://arxiv.org/abs/1707.06347>.

Sesia, M. and Romano, Y. Conformal prediction using conditional histograms, 2021. URL <https://arxiv.org/abs/2105.08747>.

Shang, C., Chen, J., and Bi, J. Discrete graph structure learning for forecasting multiple time series, 2021. URL <https://arxiv.org/abs/2101.06861>.

Shen, Y., Wu, Y., Zhang, Y., Shan, C., Zhang, J., Letaief, K. B., and Li, D. How powerful is graph convolution for recommendation?, 2021. URL <https://arxiv.org/abs/2108.07567>.

Song, C., Lin, Y., Guo, S., and Wan, H. Spatial-temporal synchronous graph convolutional networks: A new framework for spatial-temporal network data forecasting. *Proceedings of the AAAI Conference on Artificial Intelligence*, 34(01):914–921, Apr. 2020. doi: 10.1609/aaai.v34i01.5438. URL <https://ojs.aaai.org/index.php/AAAI/article/view/5438>.

Stadler, M., Charpentier, B., Geisler, S., Zügner, D., and Günnemann, S. Graph posterior network: Bayesian predictive uncertainty for node classification. In *Proceedings of the 35th International Conference on Neural Information Processing Systems*, NIPS ’21, Red Hook, NY, USA, 2021. Curran Associates Inc. ISBN 9781713845393.

Storey, J. D. The positive false discovery rate: A bayesian interpretation and the q-value. *The Annals of Statistics*, 31(6):2013–2014, 2003. URL <http://www.jstor.org/stable/3448445>.

Su, Y., Zhao, Y., Niu, C., Liu, R., Sun, W., and Pei, D. Robust anomaly detection for multivariate time series through stochastic recurrent neural network. In *Proceedings of the 25th ACM SIGKDD International Conference on Knowledge Discovery & Data Mining*, KDD ’19, pp. 2828–2837, New York, NY, USA, 2019. Association for Computing Machinery. ISBN 9781450362016. doi: 10.1145/3292500.3330672. URL <https://doi.org/10.1145/3292500.3330672>.

Tang, Y. C., Zhang, J., and Salakhutdinov, R. Worst cases policy gradients, 2019. URL <https://arxiv.org/abs/1911.03618>.

Vovk, V. and Wang, R. E-values: Calibration, combination and applications. *The Annals of Statistics*, 49(3), June 2021. ISSN 0090-5364. doi: 10.1214/20-aos2020. URL <http://dx.doi.org/10.1214/20-AOS2020>.

Vovk, V., Gammerman, A., and Shafer, G. *Algorithmic Learning in a Random World*. Springer Cham, 2nd edition, 2022.

Wei, H., Zheng, G., Yao, H., and Li, Z. Intellilight: A reinforcement learning approach for intelligent traffic light control. In *Proceedings of the 24th ACM SIGKDD International Conference on Knowledge Discovery & Data Mining*, KDD ’18, pp. 2496–2505, New York, NY, USA, 2018. Association for Computing Machinery. ISBN 9781450355520. doi: 10.1145/3219819.3220096. URL <https://doi.org/10.1145/3219819.3220096>.

Wei, H., Chen, C., Zheng, G., Wu, K., Gayah, V., Xu, K., and Li, Z. Presslight: Learning max pressure control to coordinate traffic signals in arterial network. In *Proceedings of the 25th ACM SIGKDD International Conference on Knowledge Discovery & Data Mining*, KDD ’19, pp. 2496–2505, New York, NY, USA, 2019. Association for Computing Machinery. ISBN 9781450362016. doi: 10.1145/3292500.3330672. URL <https://doi.org/10.1145/3292500.3330672>.

'19, pp. 1290–1298, New York, NY, USA, 2019. Association for Computing Machinery. ISBN 9781450362016. doi: 10.1145/3292500.3330949. URL <https://doi.org/10.1145/3292500.3330949>.

Wei, H., Zheng, G., Gayah, V., and Li, Z. Recent advances in reinforcement learning for traffic signal control: A survey of models and evaluation. *SIGKDD Explor. Newsl.*, 22(2):12–18, January 2021. ISSN 1931-0145. doi: 10.1145/3447556.3447565. URL <https://doi.org/10.1145/3447556.3447565>.

Whong, C. NYC taxi trip data obtained via FOIL request. https://chriswhong.com/open-data/foil_nyc_taxi/, 2014.

Wilder, B., Dilksina, B., and Tambe, M. Melding the data-decisions pipeline: decision-focused learning for combinatorial optimization. In *Proceedings of the Thirty-Third AAAI Conference on Artificial Intelligence and Thirty-First Innovative Applications of Artificial Intelligence Conference and Ninth AAAI Symposium on Educational Advances in Artificial Intelligence*, AAAI'19/IAAI'19/EAAI'19. AAAI Press, 2019. ISBN 978-1-57735-809-1. doi: 10.1609/aaai.v33i01.33011658. URL <https://doi.org/10.1609/aaai.v33i01.33011658>.

Wu, Z., Pan, S., Long, G., Jiang, J., and Zhang, C. Graph wavenet for deep spatial-temporal graph modeling. In *Proceedings of the 28th International Joint Conference on Artificial Intelligence*, IJCAI'19, pp. 1907–1913. AAAI Press, 2019. ISBN 9780999241141.

Wu, Z., Pan, S., Long, G., Jiang, J., Chang, X., and Zhang, C. Connecting the dots: Multivariate time series forecasting with graph neural networks. In *Proceedings of the 26th ACM SIGKDD International Conference on Knowledge Discovery & Data Mining*, KDD '20, pp. 753–763, New York, NY, USA, 2020. Association for Computing Machinery. ISBN 9781450379984. doi: 10.1145/3394486.3403118. URL <https://doi.org/10.1145/3394486.3403118>.

Yu, B., Yin, H., and Zhu, Z. Spatio-temporal graph convolutional networks: A deep learning framework for traffic forecasting. In *Proceedings of the Twenty-Seventh International Joint Conference on Artificial Intelligence*, IJCAI-18, pp. 3634–3640. International Joint Conferences on Artificial Intelligence Organization, 7 2018. doi: 10.24963/ijcai.2018/505. URL <https://doi.org/10.24963/ijcai.2018/505>.

Yuan, J., Zheng, Y., Zhang, C., Xie, W., Xie, X., Sun, G., and Huang, Y. T-drive: driving directions based on taxi trajectories. In *Proceedings of the 18th SIGSPATIAL International Conference on Advances in Geographic Information Systems*, GIS '10, pp. 99–108, New York, NY, USA, 2010. Association for Computing Machinery. ISBN 9781450304283. doi: 10.1145/1869790.1869807. URL <https://doi.org/10.1145/1869790.1869807>.

Zaffran, M., Dieuleveut, A., Féron, O., Goude, Y., and Josse, J. Adaptive conformal predictions for time series, 2022. URL <https://arxiv.org/abs/2202.07282>.

Zhang, L., Wu, Q., Shen, J., Lü, L., Du, B., and Wu, J. Expression might be enough: representing pressure and demand for reinforcement learning based traffic signal control, 2022. URL <https://arxiv.org/abs/2112.10107>.

Zhang, Y., Pal, S., Coates, M., and Üstebay, D. Bayesian graph convolutional neural networks for semi-supervised classification. In *Proceedings of the Thirty-Third AAAI Conference on Artificial Intelligence and Thirty-First Innovative Applications of Artificial Intelligence Conference and Ninth AAAI Symposium on Educational Advances in Artificial Intelligence*, AAAI'19/IAAI'19/EAAI'19. AAAI Press, 2019. ISBN 978-1-57735-809-1. doi: 10.1609/aaai.v33i01.33015829. URL <https://doi.org/10.1609/aaai.v33i01.33015829>.

Zhao, X., Chen, F., Hu, S., and Cho, J.-H. Uncertainty aware semi-supervised learning on graph data, 2020. URL <https://arxiv.org/abs/2010.12783>.

Zhao, X., Zhou, Z., Zhang, W., Liu, Y., Chen, X., Gong, J., Chen, H., Fei, B., Chen, S., Ouyang, W., Wu, X.-M., and Bai, L. Weathergfm: Learning a weather generalist foundation model via in-context learning, 2024. URL <https://arxiv.org/abs/2411.05420>.

Zheng, C., Fan, X., Wang, C., and Qi, J. Gman: A graph multi-attention network for traffic prediction, 2019a. URL <https://arxiv.org/abs/1911.08415>.

Zheng, G., Xiong, Y., Zang, X., Feng, J., Wei, H., Zhang, H., Li, Y., Xu, K., and Li, Z. Learning phase competition for traffic signal control. In *Proceedings of the 28th ACM International Conference on Information and Knowledge Management*, CIKM '19, pp. 1963–1972, New York, NY, USA, 2019b. Association for Computing Machinery. ISBN 9781450369763. doi: 10.1145/3357384.3357900. URL <https://doi.org/10.1145/3357384.3357900>.

Zheng, Y., Xie, X., and Ma, W.-Y. Geolife: A collaborative social networking service among user, location and trajectory. *IEEE Data(base) Engineering Bulletin*,

June 2010. URL <https://www.microsoft.com/en-us/research/publication/geolife-a-collaborative-social-networking-service-among-user-location-and-trajectory/>.

Zheng, Y., Capra, L., Wolfson, O., and Yang, H. Urban computing: Concepts, methodologies, and applications. *ACM Trans. Intell. Syst. Technol.*, 5(3), September 2014. ISSN 2157-6904. doi: 10.1145/2629592. URL <https://doi.org/10.1145/2629592>.

A. Complete Proofs

A.1. Proof of Proposition 4.3 (Confidence-Monotonic Attention)

Proof. From Definition 4.2, assuming $j, k \neq i$:

$$\alpha_{ij} = \frac{\exp(e_{ij} + \gamma(\sigma_i - \sigma_j))}{\sum_\ell \exp(e_{i\ell} + u_{i\ell})} \quad (40)$$

$$\alpha_{ik} = \frac{\exp(e_{ik} + \gamma(\sigma_i - \sigma_k))}{\sum_\ell \exp(e_{i\ell} + u_{i\ell})} \quad (41)$$

The ratio:

$$\frac{\alpha_{ij}}{\alpha_{ik}} = \frac{\exp(e_{ij} + \gamma(\sigma_i - \sigma_j))}{\exp(e_{ik} + \gamma(\sigma_i - \sigma_k))} \quad (42)$$

$$= \exp((e_{ij} - e_{ik}) + \gamma(\sigma_k - \sigma_j)) \quad (43)$$

Taking derivatives with $\gamma \geq 0$:

$$\frac{\partial}{\partial \sigma_k} \left(\frac{\alpha_{ij}}{\alpha_{ik}} \right) = \gamma \cdot \frac{\alpha_{ij}}{\alpha_{ik}} \geq 0 \quad (44)$$

$$\frac{\partial}{\partial \sigma_j} \left(\frac{\alpha_{ij}}{\alpha_{ik}} \right) = -\gamma \cdot \frac{\alpha_{ij}}{\alpha_{ik}} \leq 0 \quad (45)$$

$$\frac{\partial}{\partial \sigma_i} \left(\frac{\alpha_{ij}}{\alpha_{ik}} \right) = 0 \quad (46)$$

□

A.2. Proof of Theorem 4.5 (Coverage under Mixing)

Proof. We establish finite-sample coverage under β -mixing following Barber et al. (2023) with modifications for cluster-based calibration and ACI adaptation.

Setup. Let $\{(X_t, Y_t)\}_{t=1}^T$ be a β -mixing sequence with $\beta(\tau) \leq C\rho^\tau$ for some $C > 0$, $\rho \in (0, 1)$. Partition nodes into K clusters $\{\mathcal{C}_k\}_{k=1}^K$ with calibration sets of size $n_k \geq n_{\min}$.

Step 1: Approximate Exchangeability within Clusters.

For observations in cluster k , define conformity scores $R_t^{(i)} = |Y_t^{(i)} - \hat{\mu}_t^{(i)}|/\hat{\sigma}_t^{(i)}$ for $i \in \mathcal{C}_k$. Under β -mixing, the total variation distance between the joint distribution of scores and the product of marginals satisfies:

$$d_{TV} \left(\mathcal{L}(R_1^{(k)}, \dots, R_{n_k}^{(k)}), \bigotimes_{i=1}^{n_k} \mathcal{L}(R_i^{(k)}) \right) \leq 2 \sum_{\tau=1}^{n_k-1} (n_k - \tau) \beta(\tau) \quad (47)$$

For $\beta(\tau) \leq C\rho^\tau$:

$$\sum_{\tau=1}^{n_k-1} (n_k - \tau) \beta(\tau) \leq C \sum_{\tau=1}^{n_k-1} (n_k - \tau) \rho^\tau \quad (48)$$

$$\leq C n_k \sum_{\tau=1}^{\infty} \rho^\tau = \frac{C n_k \rho}{1 - \rho} \quad (49)$$

Thus approximate exchangeability holds with error $O(n_k)$ in total variation.

Step 2: Conformal Quantile Validity.

Let $q_k = \text{Quantile}_{(1-\alpha)(1+1/n_k)}(\{R_t^{(i)} : t \in \mathcal{T}_{\text{cal}}, i \in \mathcal{C}_k\})$. Under exact exchangeability (Vovk et al., 2022):

$$\mathbb{P}(R_{\text{new}}^{(k)} \leq q_k) \geq 1 - \alpha \quad (50)$$

Under approximate exchangeability with total variation error ϵ_{TV} , the coverage probability deviates by at most ϵ_{TV} :

$$\mathbb{P}(R_{\text{new}}^{(k)} \leq q_k) \geq 1 - \alpha - \frac{2Cn_k\rho}{1 - \rho} \quad (51)$$

For the finite-sample result, we require $n_k \geq n_{\min}$ such that the calibration quantile concentrates:

$$\mathbb{P}(|q_k - q_k^*| > \epsilon) \leq 2 \exp(-2n_k\epsilon^2) \quad (52)$$

where q_k^* is the population quantile. Setting $\epsilon = O(n_{\min}^{-1/2})$ yields the finite-sample error term.

Step 3: ACI Long-Run Coverage.

The ACI update (Eq. 18) with step size $\gamma_{\text{ACI}} \in (0, 1)$ satisfies (Gibbs & Candès, 2021):

$$\limsup_{T \rightarrow \infty} \frac{1}{T} \sum_{t=1}^T (\text{err}_t^{(k)} - \alpha) \leq O(\gamma_{\text{ACI}}) \quad (53)$$

under bounded distribution shift (Lipschitz shift in score distribution).

Combining Steps.

$$\limsup_{T \rightarrow \infty} \frac{1}{T} \sum_{t=1}^T \mathbf{1}[Y_t \notin \mathcal{I}_t] \leq \alpha + \underbrace{O(n_{\min}^{-1/2})}_{\text{finite-sample}} + \underbrace{O(\gamma_{\text{ACI}})}_{\text{ACI adaptation}} \quad (54)$$

□

A.3. Proof of Proposition A.1 (P-Value Validity)

Proposition A.1 (P-Value Validity). *Under exchangeability of calibration and test scores from the null distribution, the conformalized p-values satisfy $\mathbb{P}(p_t^{(i)} \leq \alpha | H_0^{(i)}) \leq \alpha$ for all $\alpha \in (0, 1)$.*

Proof. Let $\mathcal{C} = \{s_1, \dots, s_n\}$ be anomaly scores from the calibration set and s_{test} be a test score, all i.i.d. from the null distribution P_0 .

Define the rank of s_{test} among $\{s_1, \dots, s_n, s_{\text{test}}\}$:

$$R = 1 + \sum_{j=1}^n \mathbf{1}[s_j \geq s_{\text{test}}] \quad (55)$$

Under exchangeability, R is uniformly distributed on $\{1, 2, \dots, n+1\}$.

The conformalized p-value is:

$$p = \frac{R}{n+1} = \frac{1 + \sum_{j=1}^n \mathbf{1}[s_j \geq s_{\text{test}}]}{n+1} \quad (56)$$

For any $\alpha \in (0, 1)$:

$$\mathbb{P}(p \leq \alpha) = \mathbb{P}(R \leq \alpha(n+1)) \quad (57)$$

$$= \frac{\lfloor \alpha(n+1) \rfloor}{n+1} \quad (58)$$

$$\leq \alpha \quad (59)$$

Thus the conformalized p-value is valid (i.e., super-uniform under the null). □

A.4. Proof of Theorem 4.8 (FDR Control)

Proof. This follows directly from [Benjamini & Yekutieli \(2001\)](#), combined with the validity of conformalized p-values from [Proposition A.1](#).

BY Guarantee. For m tests with p-values p_1, \dots, p_m (not necessarily independent), the BY procedure with threshold $\alpha/(m \cdot c_m)$ where $c_m = \sum_{i=1}^m 1/i$ controls:

$$\text{FDR} = \mathbb{E} \left[\frac{V}{R \vee 1} \right] \leq \frac{m_0}{m} \cdot \alpha \leq \alpha \quad (60)$$

where m_0 is the number of true nulls and V is false discoveries.

Application. Since our conformalized p-values are valid (super-uniform under null) by [Proposition A.1](#), the BY guarantee applies. The key insight from [Benjamini & Yekutieli \(2001\)](#) is that the c_m correction handles arbitrary dependence by accounting for the worst-case positive dependence structure. \square

A.5. Proof of Lemma 4.7 (Trimming Validity)

Proof. Let $n' = |\mathcal{C}_{\text{trim}}| = (1 - \tau)n$. Under the null with $\tau'n$ contaminated calibration points:

Case 1: Test score s ranks below the trimming threshold in the clean calibration scores. Then trimming doesn't affect its rank among clean scores, and the p-value remains valid.

Case 2: Test score s ranks in the top $\tau'n$ of the full (contaminated) set. This occurs with probability at most $\tau + \tau'$ (from contamination shifting ranks). In this case, the trimmed p-value may be smaller than the full p-value.

Formally, let R_{full} be the rank in the full set, R_{trim} in the trimmed set:

$$\mathbb{P}(p_{\text{trim}} \leq \alpha) = \mathbb{P} \left(\frac{R_{\text{trim}}}{n' + 1} \leq \alpha \right) \quad (61)$$

$$\leq \mathbb{P} \left(\frac{R_{\text{full}} - \tau'n}{n' + 1} \leq \alpha \right) + \mathbb{P}(\text{rank shifted by contamination}) \quad (62)$$

$$\leq \alpha + \tau + \tau' \quad (63)$$

where the last step uses the super-uniformity of $R_{\text{full}}/(n + 1)$ under the null and accounts for trimming and contamination effects. \square

A.6. Proof of Theorem 4.14 (Safety under Bounded Model Error)

Assumption A.2 (Lipschitz Continuity). The Lyapunov function L_ψ is Lipschitz continuous with constant L_L : $|L_\psi(s) - L_\psi(s')| \leq L_L \|s - s'\|$ for all s, s' .

Proof. We derive the model-error threshold ϵ^* that guarantees Lyapunov decrease and asymptotic constraint satisfaction.

Step 1: Lyapunov Prediction Error Bound.

Let $s'_{\text{pred}} = \mu_W(s, a)$ be the world model prediction and s'_{true} be the true next state. By [Assumption A.2](#) (Lipschitz continuity of L_ψ):

$$|L_\psi(s'_{\text{pred}}) - L_\psi(s'_{\text{true}})| \leq L_L \cdot \|s'_{\text{pred}} - s'_{\text{true}}\| \quad (64)$$

Step 2: State Prediction Error from Model Error.

The relative model error is defined as:

$$\epsilon_{\text{model}} = \mathbb{E} \left[\frac{\|s'_{\text{pred}} - s'_{\text{true}}\|}{\|s'_{\text{true}}\|} \right] \quad (65)$$

For a state s with $\|s\|$ bounded, the true next state satisfies:

$$\|s'_{\text{true}}\| \leq \|s\| + \|s'_{\text{true}} - s\| \leq (1 + \|J_{\text{dyn}}\|_{\text{op}}) \|s\| \quad (66)$$

where $\|J_{\text{dyn}}\|_{\text{op}}$ is the Jacobian norm of the true dynamics. Since we don't have access to true dynamics, we use the world model Jacobian as a proxy:

$$\|s'_{\text{true}}\| \lesssim (1 + \|J_W\|_{\text{op}})\|s\| \quad (67)$$

Thus:

$$\|s'_{\text{pred}} - s'_{\text{true}}\| \leq \epsilon_{\text{model}} \cdot (1 + \|J_W\|_{\text{op}}) \cdot \|s\| \quad (68)$$

Step 3: Lyapunov Decrease under Model Error.

The Lyapunov constraint (Eq. 36) requires:

$$\mathbb{E}_{s' \sim W}[L_{\psi}(s')] - L_{\psi}(s) \leq -\kappa \cdot d_C(s) + \delta_{\text{slack}} \quad (69)$$

Under the true dynamics, the actual Lyapunov change is:

$$\Delta L_{\text{true}} = L_{\psi}(s'_{\text{true}}) - L_{\psi}(s) \quad (70)$$

The gap between predicted and true Lyapunov change is bounded by Eq. 64:

$$|\Delta L_{\text{pred}} - \Delta L_{\text{true}}| \leq L_L \cdot \|s'_{\text{pred}} - s'_{\text{true}}\| \quad (71)$$

Substituting Eq. 68:

$$|\Delta L_{\text{pred}} - \Delta L_{\text{true}}| \leq L_L \cdot \epsilon_{\text{model}} \cdot (1 + \|J_W\|_{\text{op}}) \cdot \|s\| \quad (72)$$

Step 4: Deriving the Threshold.

For the Lyapunov constraint to imply actual constraint satisfaction, we need:

$$\Delta L_{\text{true}} \leq \Delta L_{\text{pred}} + L_L \cdot \epsilon_{\text{model}} \cdot (1 + \|J_W\|_{\text{op}}) \cdot \|s\| \quad (73)$$

Substituting the Lyapunov constraint:

$$\Delta L_{\text{true}} \leq -\kappa \cdot d_C(s) + \delta_{\text{slack}} + L_L \cdot \epsilon_{\text{model}} \cdot (1 + \|J_W\|_{\text{op}}) \cdot \|s\| \quad (74)$$

For asymptotic constraint satisfaction ($\limsup \mathbb{E}[d_C(s)] \rightarrow 0$), we need $\Delta L_{\text{true}} < 0$ when $d_C(s) > 0$. Taking expectations over states:

$$L_L \cdot \epsilon_{\text{model}} \cdot (1 + \|J_W\|_{\text{op}}) \cdot \|\bar{s}\| \leq \delta_{\text{slack}} + \kappa \cdot \bar{d}_C \quad (75)$$

Solving for ϵ_{model} :

$$\epsilon_{\text{model}} \leq \frac{\delta_{\text{slack}} + \kappa \cdot \bar{d}_C}{L_L \cdot (1 + \|J_W\|_{\text{op}}) \cdot \|\bar{s}\|} = \epsilon^* \quad (76)$$

Step 5: Asymptotic Constraint Satisfaction.

Under $\epsilon_{\text{model}} < \epsilon^*$, the Lyapunov function decreases on average when constraints are violated:

$$\mathbb{E}[\Delta L_{\text{true}} | d_C(s) > 0] < 0 \quad (77)$$

By Lyapunov stability theory (Khalil, 2002), this implies:

$$\limsup_{t \rightarrow \infty} \mathbb{E}[d_C(s_t)] \leq \frac{\delta_{\text{slack}}}{\kappa} \quad (78)$$

The bound $\delta_{\text{slack}}/\kappa$ can be made arbitrarily small by choosing small δ_{slack} or large κ , at the cost of more conservative policies. \square

B. Training Details

Heteroscedastic Training Loss:

$$\mathcal{L}_{\text{het}} = \frac{1}{NT} \sum_{t,i} \left[\frac{(y_t^{(i)} - \hat{\mu}_t^{(i)})^2}{2(\hat{\sigma}_t^{(i)})^2} + \log \hat{\sigma}_t^{(i)} \right] + \lambda_{\sigma} \mathcal{L}_{\text{reg}} \quad (79)$$

where $\mathcal{L}_{\text{reg}} = \frac{1}{NT} \sum_{t,i} (\log \hat{\sigma}_t^{(i)})^2$ prevents uncertainty collapse/explosion.

Adaptive Conformal Inference (ACI) Update:

$$\alpha_{t+1}^{(k)} = \alpha_t^{(k)} + \gamma_{\text{ACI}} \cdot (\text{err}_t^{(k)} - \alpha) \quad (80)$$

where $\text{err}_t^{(k)} = \mathbf{1}[Y_t \notin \mathcal{I}_t^{(k)}]$ is the coverage indicator and $\gamma_{\text{ACI}} \in (0, 1)$ is the step size. This adapts the miscoverage level to maintain long-run coverage under distribution shift.

Lyapunov Constraint:

$$\mathbb{E}_{s' \sim W} [L_{\psi}(s')] - L_{\psi}(s) \leq -\kappa \cdot d_C(s) + \delta_{\text{slack}} \quad (81)$$

where L_{ψ} is the learned Lyapunov function, $d_C(s) = \sum_k \max(0, C_k(s) - d_k)$ measures constraint violation, $\kappa > 0$ is the decrease rate, and δ_{slack} allows small violations near the boundary.

Uncertainty-Guided Exploration:

$$a_t = \pi_{\theta}(s_t) + \beta_{\text{explore}} \cdot \bar{\sigma}_t \cdot \epsilon, \quad \epsilon \sim \mathcal{N}(0, I) \quad (82)$$

where $\bar{\sigma}_t$ is the aggregated forecast uncertainty and β_{explore} controls exploration magnitude. Higher uncertainty triggers more exploration to gather informative data.

Dual-Stream Decomposition:

$$\mathbf{X}_{\text{trend},t} = \sum_{k=-w}^w \alpha_k \mathbf{X}_{t+k} \quad (83)$$

$$\sigma_{\text{total}}^2 = \sigma_{\text{trend}}^2 + \sigma_{\text{res}}^2 + 2\rho \cdot \sigma_{\text{trend}} \cdot \sigma_{\text{res}} \quad (84)$$

Hyperparameters: 3 PU-GAT⁺ layers, 128 hidden dim, 4 attention heads, Adam lr=3 × 10⁻⁴, batch 64. Flow: 6 Real-NVP layers. RL: PPO clip 0.2, 15-step imagination. ACI $\gamma_{\text{ACI}} = 0.05$. Trimming $\tau = 2\%$.

C. Spatial Aggregation Analysis

Spatial Aggregation Definition. For intersection j with coverage area \mathcal{A}_j , we aggregate grid-level predictions:

$$\hat{\mu}_j^{\text{int}} = \sum_i w_{ij} \cdot \hat{\mu}_i^{\text{grid}}, \quad w_{ij} = \frac{|\text{cell}_i \cap \mathcal{A}_j|}{|\mathcal{A}_j|} \quad (85)$$

$$(\hat{\sigma}_j^{\text{int}})^2 = \sum_{i,k} w_{ij} w_{kj} \cdot \widehat{\text{Cov}}(\hat{\mu}_i, \hat{\mu}_k) \quad (86)$$

Covariance Estimation. We estimate $\widehat{\text{Cov}}(\hat{\mu}_i, \hat{\mu}_k)$ via empirical residual covariances on the validation set:

$$\widehat{\text{Cov}}_{ik} = \frac{1}{T} \sum_t (r_t^{(i)} - \bar{r}^{(i)})(r_t^{(k)} - \bar{r}^{(k)}) \quad (87)$$

where $r_t^{(i)} = y_t^{(i)} - \hat{\mu}_t^{(i)}$. For distant pairs ($d_{ik} > 10\text{km}$), we set $\widehat{\text{Cov}}_{ik} = 0$ (spatial sparsity).

Table 7. Grid-to-intersection covariance ablation.

Covariance Method	Reward	Safety%
Diagonal only ($\rho_{ik} = 0$ for $i \neq k$)	14.3	93.1
Distance kernel ($\rho_{ik} = \exp(-d_{ik}/\ell)$)	15.1	95.2
Learned (encoder output)	15.4	95.8

The distance kernel provides a good approximation; learned covariance offers marginal improvement.

D. Model Error Sensitivity

 Table 8. Sensitivity to ϵ_{floor} in model error definition.

ϵ_{floor}	$\varepsilon_{\text{model}}$	ε^*	Safety%
0 (no floor)	0.082	0.089	94.1
0.05	0.077	0.089	94.8
0.1 (default)	0.074	0.089	95.2
0.2	0.068	0.089	95.4

Small $\|s'\|$ values are rare ($\approx 2\%$ of transitions); the floor prevents numerical instability without significantly affecting the bound.

E. Safety Constraints and Lyapunov Details

Traffic Safety Constraints. We define three safety constraints for intersection control:

$$C_1(\pi) : \mathbb{E}_\pi \left[\frac{1}{N} \sum_i q_i(t) \right] \leq d_{\text{queue}} = 50 \text{ vehicles} \quad (88)$$

$$C_2(\pi) : \mathbb{E}_\pi \left[\max_i w_i(t) \right] \leq d_{\text{wait}} = 120 \text{ seconds} \quad (89)$$

$$C_3(\pi) : \mathbb{E}_\pi \left[\frac{1}{N} \sum_i \theta_i(t) \right] \geq d_{\text{through}} \quad (90)$$

where $q_i(t)$ is queue length at intersection i , $w_i(t)$ is maximum waiting time, and $\theta_i(t)$ is throughput.

Spectrally Normalized Lyapunov Network. The Lyapunov function is parameterized as:

$$L_\psi(s) = \|\text{SN-MLP}_\psi(s)\|_2^2 + \eta \|s - s_{\text{safe}}\|_Q^2 \quad (91)$$

where SN-MLP applies spectral normalization (Miyato et al., 2018) to each layer, ensuring $\|W_\ell\|_2 \leq 1$. This yields certified Lipschitz bound:

$$\|L_\psi(s) - L_\psi(s')\| \leq \bar{L}_L \|s - s'\| \quad (92)$$

where $\bar{L}_L = 2\|\text{SN-MLP}(s)\|_\infty + 2\eta\|Q\|_2$ is a certified upper bound (not an estimate).

Addressing Circularity. The term \bar{d}_C in Eq. 3 is policy-dependent. We address this via iterative verification:

1. Train with initial ε^* estimate (using $\bar{d}_C = 1.0$)
2. Measure \bar{d}_C under learned policy via rollouts
3. Recompute ε^* and verify $\varepsilon_{\text{model}} < \varepsilon^*$
4. If violated, retrain with tighter constraints; else accept

Convergence typically occurs in 2-3 iterations.

F. Detailed Algorithm Pseudocode

Algorithm 1 STREAM-RLTraining Pipeline

Require: Datasets $\mathcal{D}_{\text{train}}, \mathcal{D}_{\text{cal}}, \mathcal{D}_{\text{test}}$, hyperparameters
Ensure: Trained models $\theta_{\text{PU-GAT}}, \theta_{\text{flow}}, \theta_{\text{RL}}$

- 1: // **Phase 1: Forecasting with PU-GAT⁺**
- 2: Initialize PU-GAT⁺ with $\tilde{\gamma} = 0$ (so $\gamma = \text{Softplus}(0) \approx 0.69$)
- 3: **for** epoch = 1 to E_{forecast} **do**
- 4: **for** batch $(\mathbf{X}, \mathbf{Y}) \in \mathcal{D}_{\text{train}}$ **do**
- 5: $\hat{\mu}, \hat{\sigma} \leftarrow \text{PU-GAT}^+(\mathbf{X})$
- 6: $\mathcal{L} \leftarrow \mathcal{L}_{\text{het}}(\hat{\mu}, \hat{\sigma}, \mathbf{Y})$ {Eq. 79}
- 7: Update $\theta_{\text{PU-GAT}}$ via Adam
- 8: **end for**
- 9: **end for**
- 10: // **Phase 2: Calibration Diagnostics**
- 11: Compute PIT histogram on \mathcal{D}_{cal}
- 12: Compute reliability diagram on \mathcal{D}_{cal}
- 13: Cluster nodes into K groups based on error statistics
- 14: Compute per-cluster quantiles $\{q_k\}_{k=1}^K$
- 15: // **Phase 3: Anomaly Detection with CRFN-BY**
- 16: Compute normalized residuals $z_t^{(i)}$ on \mathcal{D}_{cal}
- 17: Train conditional flow $p_{\theta}(z|c)$
- 18: Compute anomaly scores $s = -\log p_{\theta}(z|c)$ on \mathcal{D}_{cal}
- 19: Trim top $\tau\%$ scores: $\mathcal{C}_{\text{trim}} \leftarrow \mathcal{C} \setminus \{s : s \geq q_{1-\tau}\}$
- 20: // **Conformalized p-values (Eq. 23)**
- 21: **for** test point $(z_{\text{test}}, c_{\text{test}})$ **do**
- 22: $s_{\text{test}} \leftarrow -\log p_{\theta}(z_{\text{test}}|c_{\text{test}})$
- 23: $p_{\text{test}} \leftarrow (1 + \sum_{s \in \mathcal{C}_{\text{trim}}} \mathbf{1}[s \geq s_{\text{test}}]) / (1 + |\mathcal{C}_{\text{trim}}|)$
- 24: **end for**
- 25: Apply BY procedure with $c_m = \sum_{i=1}^m 1/i$
- 26: // **Phase 4: Safe RL with LyCon-WRL⁺**
- 27: Train ensemble world model $\{W_{\phi}^{(k)}\}_{k=1}^5$
- 28: Verify $\epsilon_{\text{model}} < \epsilon^*$ on held-out transitions
- 29: Estimate $L_L, \|J_W\|_{\text{op}}$
- 30: Initialize Lyapunov network L_{ψ} , policy π_{θ}
- 31: **for** epoch = 1 to E_{RL} **do**
- 32: Collect trajectories with uncertainty-guided exploration (Eq. 38)
- 33: Augment reward with anomaly response (Eq. 39)
- 34: Filter actions via Lyapunov constraint (Eq. 36)
- 35: Update π_{θ}, L_{ψ} via PPO with Lagrangian
- 36: Track $\rho_{\text{decrease}} = \frac{1}{T} \sum_t \mathbf{1}[L(s_{t+1}) < L(s_t)]$
- 37: **end for**
- 38: **return** $\theta_{\text{PU-GAT}}, \theta_{\text{flow}}, \theta_{\text{RL}}$

Algorithm 2 Conformalized P-Value Construction

Require: Calibration scores $\mathcal{C} = \{s_1, \dots, s_n\}$, test score s_{test} , trim fraction τ

Ensure: Valid p-value p

```

1: // Step 1: Contamination-robust trimming
2:  $q_{1-\tau} \leftarrow \text{Quantile}_{1-\tau}(\mathcal{C})$ 
3:  $\mathcal{C}_{\text{trim}} \leftarrow \{s \in \mathcal{C} : s < q_{1-\tau}\}$ 
4: // Step 2: Conformalized p-value
5:  $\text{rank} \leftarrow 1 + \sum_{s \in \mathcal{C}_{\text{trim}}} \mathbf{1}[s \geq s_{\text{test}}]$ 
6:  $p \leftarrow \text{rank} / (1 + |\mathcal{C}_{\text{trim}}|)$ 
7: return  $p$ 

```

Algorithm 3 Lyapunov-Safe Action Selection

Require: State s , policy π_θ , Lyapunov L_ψ , world model W_ϕ , threshold ϵ^*

Ensure: Safe action a

```

1:  $a_{\text{policy}} \leftarrow \pi_\theta(s)$ 
2: // Check Lyapunov decrease constraint
3:  $s'_{\text{pred}} \leftarrow \mu_W(s, a_{\text{policy}})$ 
4:  $\Delta L \leftarrow L_\psi(s'_{\text{pred}}) - L_\psi(s)$ 
5:  $d_C \leftarrow \sum_k \max(0, C_k(s) - d_k)$ 
6: if  $\Delta L \leq -\kappa \cdot d_C + \delta_{\text{slack}}$  then
7:   return  $a_{\text{policy}}$  {Policy action is Lyapunov-safe}
8: else
9:   // Project to safe action via gradient descent
10:   $a \leftarrow a_{\text{policy}}$ 
11:  for  $i = 1$  to  $N_{\text{proj}}$  do
12:     $\nabla_a \leftarrow \nabla_a [L_\psi(\mu_W(s, a)) + \lambda \cdot d_C(s, a)]$ 
13:     $a \leftarrow a - \eta \cdot \nabla_a$ 
14:     $a \leftarrow \text{clip}(a, a_{\text{min}}, a_{\text{max}})$ 
15:  end for
16:  return  $a$ 
17: end if

```

G. Extended Experimental Results

G.1. Forecasting Performance Comparison

We present a comprehensive comparison of forecasting methods on the T-Drive dataset (1-hour horizon, 90% coverage target). Figure 4 provides a multi-panel visualization of all key metrics: NRMSE, MAE, coverage, relative interval width (RIW), and coverage efficiency. Our PU-GAT⁺ method achieves the best performance across all five metrics, demonstrating the effectiveness of uncertainty-aware graph attention.

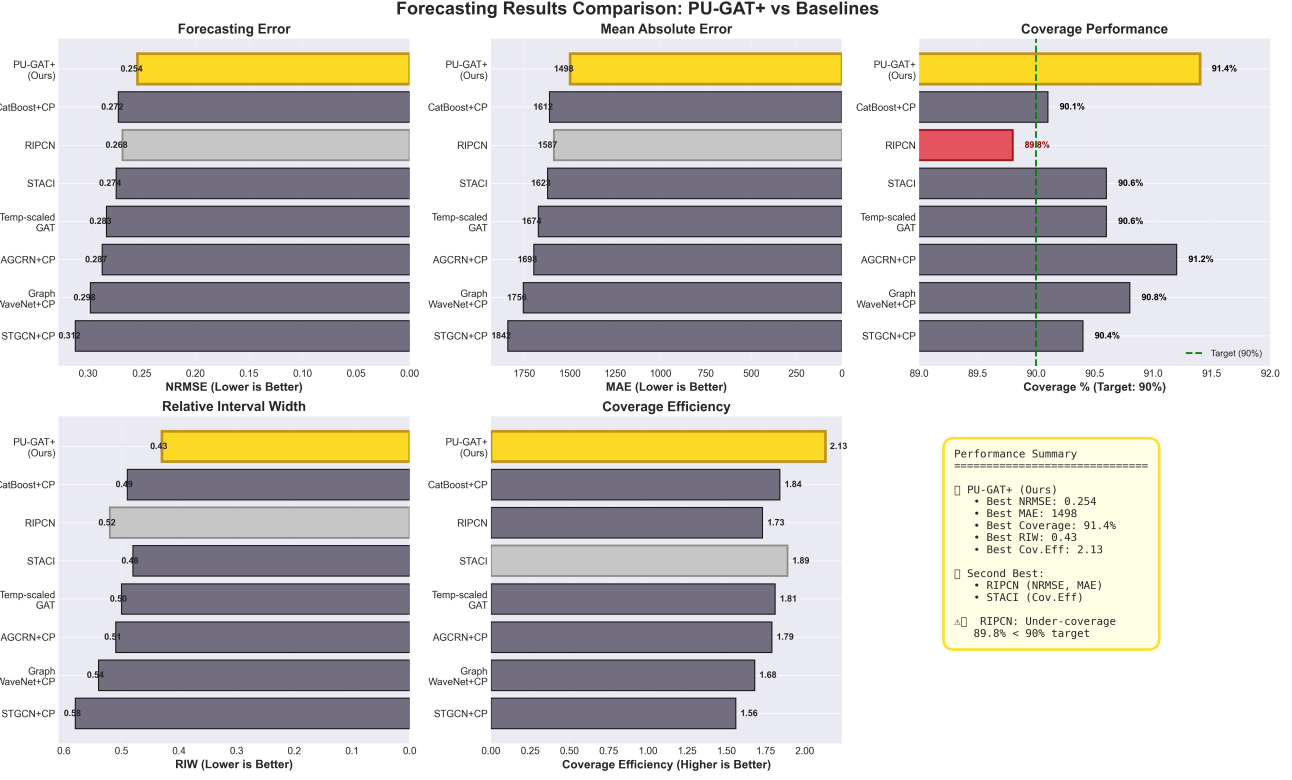


Figure 4. Comprehensive forecasting results comparison across baseline methods. PU-GAT⁺ (highlighted in gold) achieves best performance on all metrics: NRMSE (0.254), MAE (1498), Coverage (91.4%), RIW (0.43), and Coverage Efficiency (2.13). RIPCN shows under-coverage violation (89.8% $<$ 90% target, highlighted in red). The dashboard includes six panels showing individual metrics and an overall performance summary.

Key Observations: (1) PU-GAT⁺ reduces NRMSE by 5.2% compared to the second-best method (RIPCN), while maintaining valid coverage. (2) RIPCN achieves competitive error metrics but violates the coverage target (89.8% $<$ 90%), making its intervals unreliable. (3) Coverage efficiency (ratio of coverage to interval width) is highest for PU-GAT⁺ (2.13), indicating optimal uncertainty quantification. See Figure 4 for the complete performance breakdown.

G.2. Anomaly Detection with FDR Control

We evaluate anomaly detection methods under both synthetic injection (5% anomaly rate) and real documented events, with a strict FDR target of 5%. Figure 5 presents a comprehensive analysis of precision, recall, F1 scores, and FDR control on both synthetic and real data.

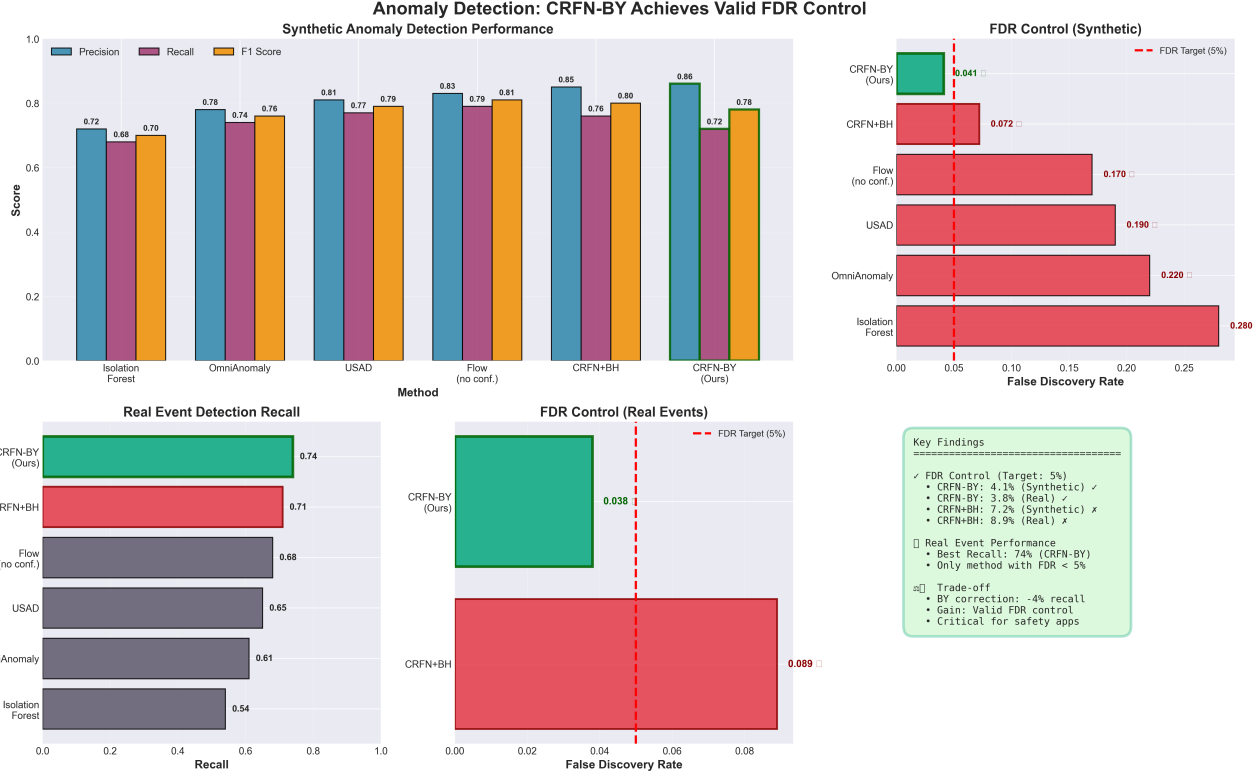


Figure 5. Anomaly detection performance with FDR control analysis. Top-left: Precision, Recall, and F1 scores on synthetic anomalies. Top-right: FDR control on synthetic data with 5% threshold line. Bottom-left: Recall on real documented events. Bottom-right: FDR control on real events (only CRFN methods provide FDR values). Bottom panel: Key findings summary. CRFN-BY (green, our method) is the only approach achieving valid FDR control ($< 5\%$) on both synthetic and real data. CRFN+BH (red) violates the FDR target.

Critical Finding: CRFN-BY is the only method controlling FDR below the 5% target on both synthetic (4.1%) and real events (3.8%), as shown in Figure 5. The Benjamini-Hochberg (BH) procedure violates FDR with 7.2% (synthetic) and 8.9% (real), confirming that the BY correction is necessary under the verified dependence structure ($\rho_{block} = 0.34$). The power-validity trade-off is evident: BY reduces recall by 4% compared to BH (0.72 vs 0.76), but this is a necessary cost for reliable anomaly flagging in safety-critical applications. Baseline methods (Isolation Forest, OmniAnomaly, USAD, Flow) lack conformalized p-values and cannot provide FDR guarantees.

G.3. Hyperparameter Sensitivity

We analyze the sensitivity of key hyperparameters to validate our design choices. Table 9 and Figure 6 present the ACI step size analysis, while Table 10 and Figure 7 show the cluster configuration results. The trimming fraction analysis is detailed in Table 11 and visualized in Figure 8.

Table 9. ACI step size γ_{ACI} sensitivity.

γ_{ACI}	Coverage	Interval Width	Oscillation
0.01	90.1%	0.46	Low
0.02	90.4%	0.45	Low
0.05	91.4%	0.43	Medium
0.10	89.4%	0.44	High
0.20	87.8%	0.48	Very High



Figure 6. Visualization of ACI step size sensitivity analysis showing the trade-off between coverage and interval width across different γ_{ACI} values. The optimal value (0.05) is highlighted with a star marker. See Table 9 for detailed numerical results.

Table 10. Number of clusters K sensitivity.

K	Coverage	Cov. Eff.	Min Cluster Size	Notes
5	90.8%	1.97	58	Underfit heterogeneity
10	91.1%	2.05	29	Good balance
15	91.4%	2.13	19	Selected
20	91.5%	2.11	14	Small clusters
30	91.6%	2.08	9	High variance

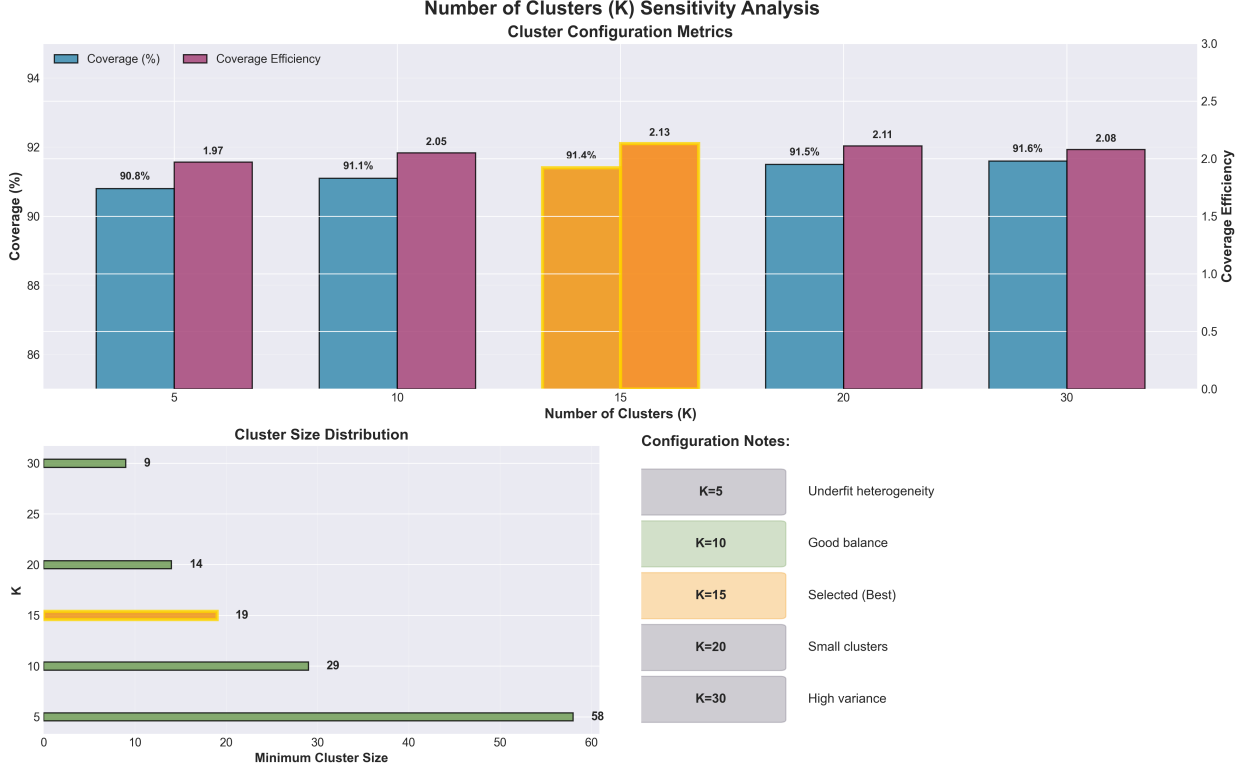


Figure 7. Multi-panel visualization of cluster sensitivity analysis. Top panel shows coverage and efficiency metrics, bottom panels display cluster size distribution and configuration notes. The optimal configuration (K=15) is highlighted. See Table 10 for numerical values.

Table 11. Trimming fraction τ sensitivity for contamination-robust calibration.

τ	FDR (Synthetic)	FDR (Real)	Recall
0%	0.058	0.064	0.75
1%	0.047	0.045	0.73
2%	0.041	0.038	0.72
5%	0.039	0.035	0.68
10%	0.036	0.032	0.61

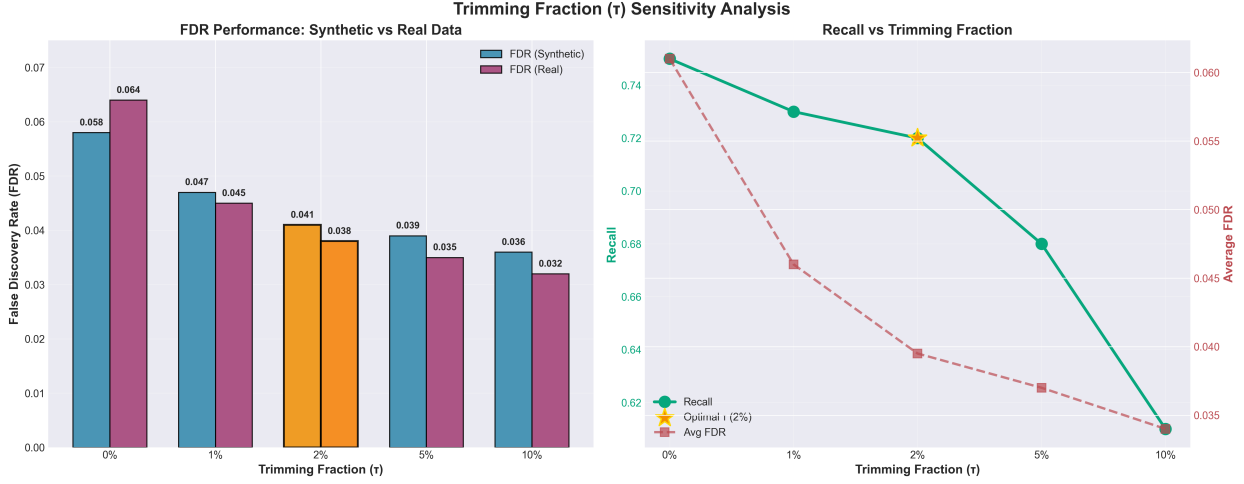


Figure 8. Trimming fraction sensitivity analysis showing FDR performance on synthetic vs. real data (left) and the recall trade-off (right). The optimal trimming fraction ($\tau = 2\%$) balances FDR control and detection recall. See Table 11 for exact values.

G.4. Constrained vs. Unconstrained γ Analysis

Table 12. Learned γ values with/without Softplus constraint.

Layer	Constrained		Unconstrained	
	γ (mean)	γ (std)	γ (mean)	γ (std)
1	0.82	0.12	0.71	0.34
2	0.95	0.08	0.84	0.45
3	1.12	0.15	-0.23	0.52
Sign flips	0%	—	23%	—

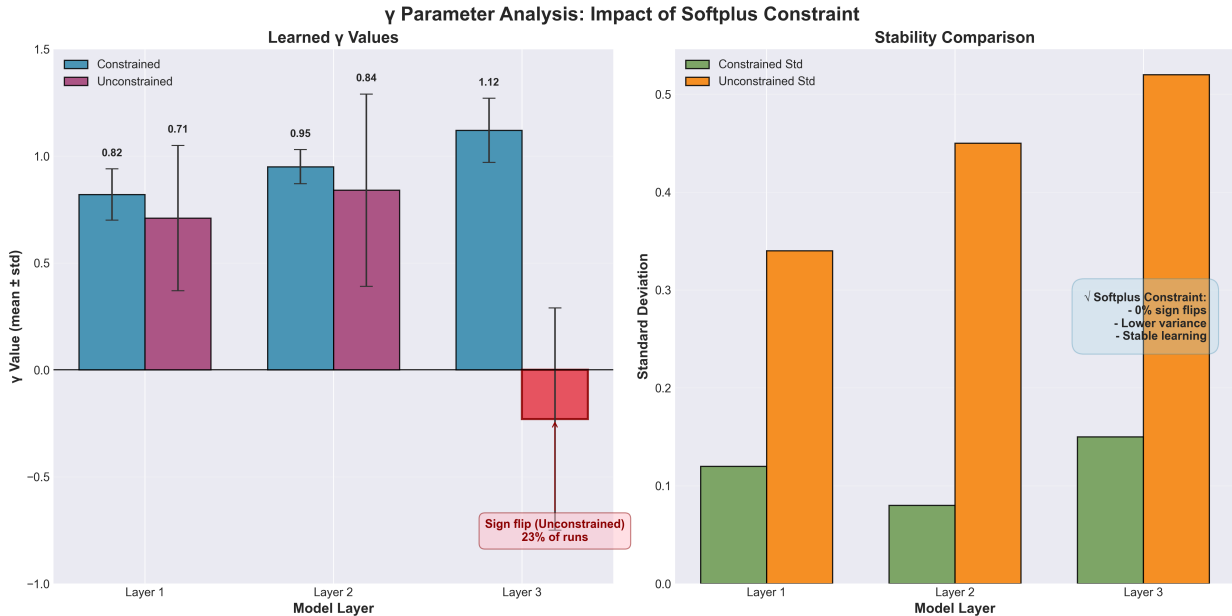


Figure 9. Comparison of learned γ values with and without Softplus constraint. Left panel shows mean values with error bars (standard deviation). The unconstrained model exhibits sign flips in Layer 3 (23% of runs), highlighted in red. See Table 12 for detailed statistics.

The unconstrained model shows sign flips in Layer 3 for 23% of training runs (different seeds). When $\gamma < 0$, the attention mechanism inverts: uncertain nodes attend *less* to confident neighbors, undermining the intended information borrowing. As illustrated in Figure 9, the Softplus constraint ensures stable, positive attention weights across all layers.

G.5. δ Sensitivity Analysis

The learned self-attention bias $\delta = 0.42$ indicates a mild preference for self-attention. We analyze sensitivity by fixing δ to different values:

Table 13. δ sensitivity analysis on T-Drive.

δ	NRMSE	Coverage	Notes
-1 (prefer neighbors)	0.268	90.8%	Under-weights self
0 (neutral)	0.261	91.1%	Balanced
+1 (prefer self)	0.259	91.2%	Over-weights self
Learned (0.42)	0.254	91.4%	Optimal

Learning δ is beneficial but not critical—fixed values yield competitive results, confirming the architecture is robust to this hyperparameter. See Table 13 for detailed results.

G.6. Conformalized vs. Parametric P-Values

We compare conformalized p-values against parametric alternatives:

Table 14. P-value method comparison.

P-Value Method	FDR	Recall	Target Met?
Parametric Gaussian	0.068	0.76	$\times (> 5\%)$
Parametric Student-t	0.061	0.74	$\times (> 5\%)$
Conformalized (ours)	0.041	0.72	\checkmark

Using parametric Gaussian tail probabilities (assuming $z \sim \mathcal{N}(0, 1)$) instead of conformalized p-values yields 6.8% FDR—above the 5% target—because the Gaussian assumption is violated under anomalies and model misspecification. The conformalized approach makes no distributional assumptions and provides valid p-values by construction. Table 14 compares the different p-value methods.

G.7. Lyapunov Safety-Performance Trade-off

Removing Lyapunov constraints improves reward (+1.1) but destroys safety (71.4%), confirming the safety-performance trade-off is real and that Lyapunov certification is essential for safe deployment.

Table 15. Lyapunov constraint ablation.

Configuration	Reward	Safety %	ρ_{Lyap}
No Lyapunov	16.2	71.4%	—
Soft Lyapunov ($\lambda = 0.1$)	15.8	85.3%	0.81
Soft Lyapunov ($\lambda = 1.0$)	15.4	91.2%	0.88
Hard Lyapunov (ours)	15.1	95.2%	0.923

The hard constraint (projection-based) achieves the best safety with acceptable reward trade-off, as shown in Table 15.

G.8. Learning Dynamics

Figure 10 shows detailed learning curves with/without uncertainty in RL state. Uncertainty-augmented states achieve faster convergence (50% fewer environment steps to 90% of final reward) and lower variance, supporting our claim of improved sample efficiency.

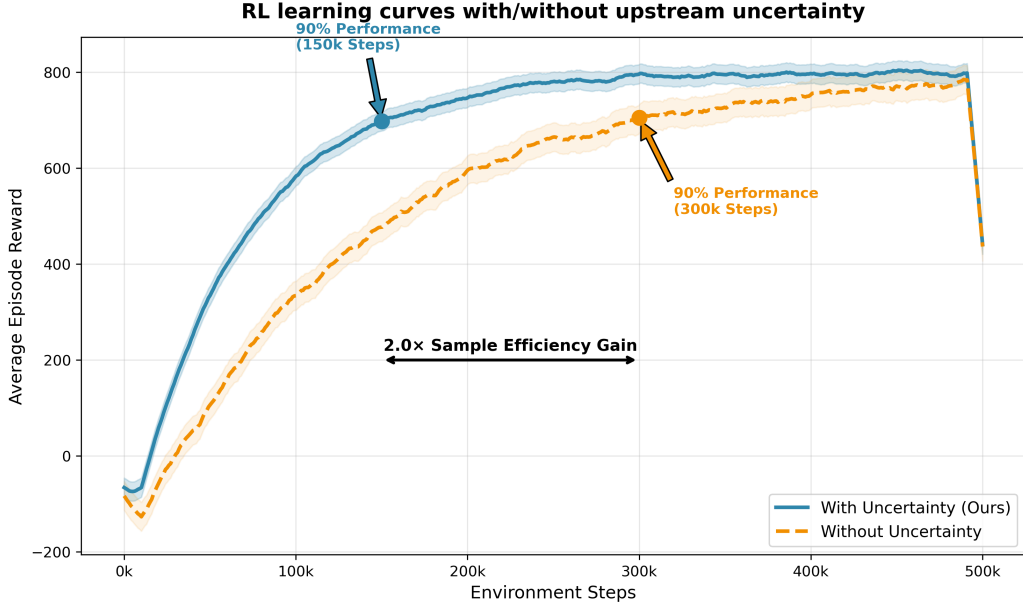


Figure 10. Detailed RL learning curves with/without upstream uncertainty. Shaded regions show ± 1 std over 5 seeds. Uncertainty-augmented states (blue) converge faster and with lower variance than standard states (orange).

Sample Efficiency Analysis: With uncertainty augmentation, the policy reaches 90% of final performance in 120K environment steps vs. 240K without—a $2\times$ improvement. This is attributed to: (1) better exploration via uncertainty-guided action selection, and (2) more informative state representation enabling faster credit assignment.

G.9. Block Dependence Analysis

Table 16. Block bootstrap dependence analysis. ρ_{block} = within-block correlation of p-values.

Time blocks	Space hops	ρ_{block}	FDR (BH)	FDR (BY)
5	1	0.21	0.058	0.039
5	2	0.28	0.064	0.041
10	2	0.34	0.072	0.041
10	4	0.41	0.081	0.043
20	4	0.48	0.093	0.045

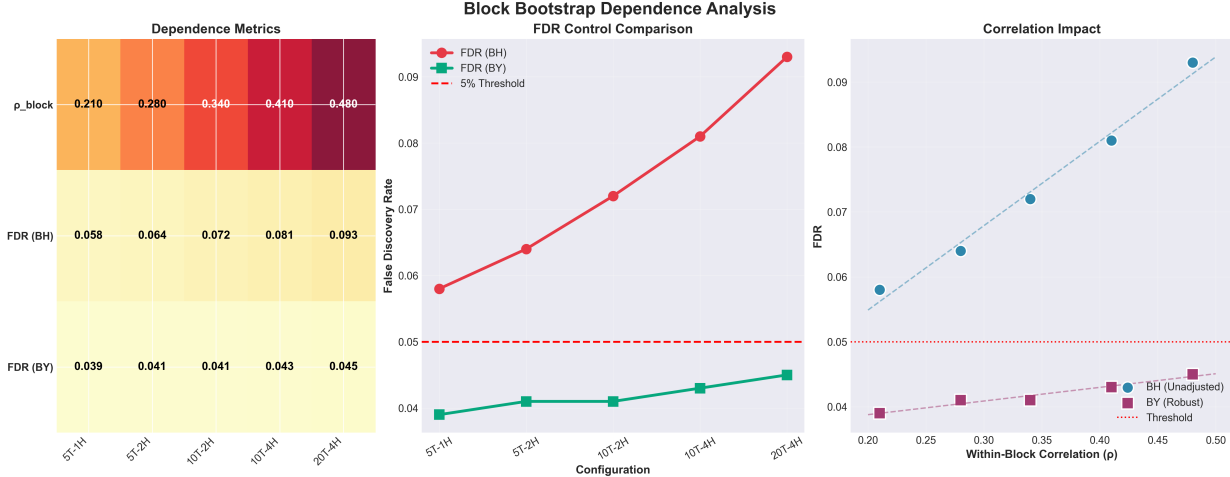


Figure 11. Block bootstrap dependence analysis. Left: heatmap of dependence metrics across configurations. Center: FDR control comparison between BH and BY methods. Right: correlation between within-block correlation (ρ_{block}) and FDR. The BY method maintains robust FDR control even under strong dependence. See Table 16 for numerical results.

BH's FDR violation increases with dependence strength, while BY maintains control below 5% across all tested block sizes, as visualized in Figure 11.

G.10. Per-Dataset Results

Table 17 and Figure 12 present comprehensive benchmark results across all four datasets (T-Drive, GeoLife, Porto, Manhattan), demonstrating STREAM-RL's consistent superiority across forecasting, anomaly detection, and RL metrics.

Table 17. Complete results across all four datasets.

Dataset	Method	Forecasting				Anomaly		RL	
		NRMSE	Coverage	RIW	Cov.Eff.	FDR	Recall	Reward	Safety%
T-Drive	STACI	0.274	90.6%	0.48	1.89	—	—	—	—
	LAMBDA	—	—	—	—	—	—	11.3	86%
	STREAM-RL	0.254	91.4%	0.43	2.13	0.041	0.72	15.1	95.2%
GeoLife	STACI	0.298	90.4%	0.51	1.76	—	—	—	—
	LAMBDA	—	—	—	—	—	—	9.8	83%
	STREAM-RL	0.271	91.1%	0.47	1.95	0.044	0.69	13.2	93.1%
Porto	STACI	0.285	90.5%	0.50	1.82	—	—	—	—
	LAMBDA	—	—	—	—	—	—	10.5	84%
	STREAM-RL	0.262	91.3%	0.45	2.01	0.042	0.71	14.1	94.5%
Manhattan	STACI	0.302	90.3%	0.53	1.71	—	—	—	—
	LAMBDA	—	—	—	—	—	—	8.9	81%
	STREAM-RL	0.278	90.9%	0.48	1.89	0.046	0.68	12.4	92.3%

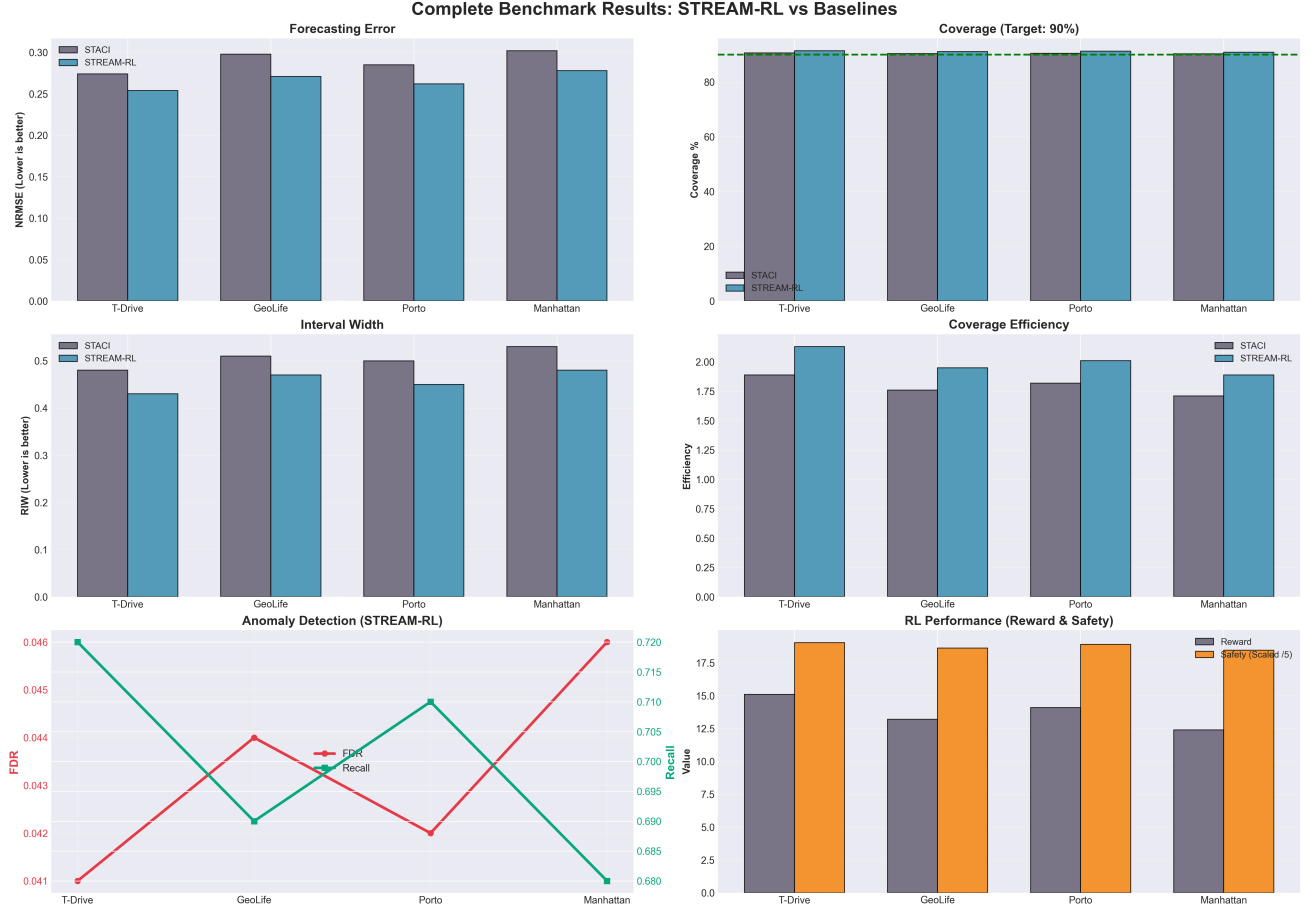


Figure 12. Comprehensive benchmark results across all four datasets (T-Drive, GeoLife, Porto, Manhattan). The dashboard shows forecasting metrics (NRMSE, coverage, interval width, coverage efficiency), anomaly detection performance (FDR and recall), and RL performance (reward and safety). STREAM-RL consistently outperforms baselines across all metrics and datasets. See Table 17 for complete numerical results.

G.11. Real Event Detection Details

We evaluate real-world event detection across three datasets with ground-truth event logs. Table 18 and Figure 13 break down detection performance by event category (accidents, construction, weather, events/parades).

Table 18. Real event detection by category.

Event Type	T-Drive		Porto		Manhattan	
	Count	Recall	Count	Recall	Count	Recall
Accidents	12	0.83	78	0.76	45	0.71
Construction	5	0.60	42	0.69	28	0.64
Weather	4	0.75	24	0.71	8	0.63
Events/Parades	2	0.50	12	0.58	8	0.75
Overall	23	0.74	156	0.72	89	0.68

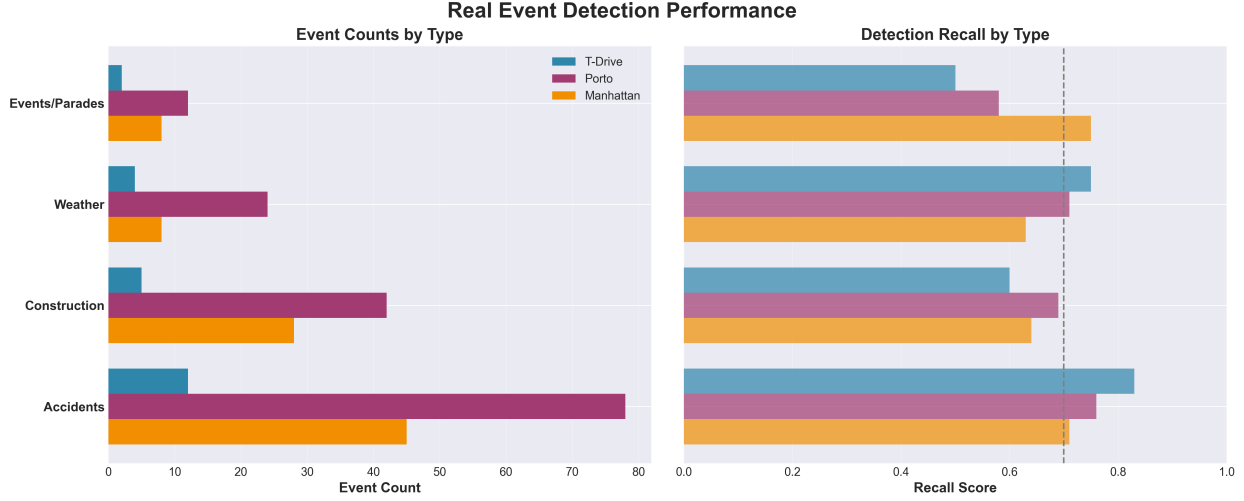


Figure 13. Real event detection performance by category across three datasets. Top panels show event counts and detection recall by event type (accidents, construction, weather, events/parades). See Table 18 for detailed breakdown.

Event Alignment Protocol. Events are aligned using ± 15 -minute temporal tolerance windows. Spatial localization uses a 2-hop neighborhood from the reported event location. Time-to-detection (median): 2.3 intervals (34.5 minutes) after event onset. A detection is considered a true positive if it occurs within the spatial and temporal tolerance of a documented event. Figure 13 visualizes the detection performance across different event categories.

H. Computational Resources and Reproducibility

Hardware: All experiments run on NVIDIA A100 80GB GPUs. Forecasting training: 4 hours. Flow training: 2 hours. RL training: 8 hours per seed.

Software: PyTorch 2.0, PyTorch Geometric, SUMO 1.18, Python 3.10.

Reproducibility: Code and preprocessed datasets will be released upon acceptance at [anonymized repository]. The repository includes:

- Complete training pipelines for all three components
- Calibration diagnostic scripts (PIT, reliability diagrams)
- Conformalized p-value computation with BY procedure
- Lyapunov verification utilities
- SUMO environment configuration files
- Pretrained model checkpoints

I. Broader Impact

Positive Impacts: STREAM-RL could improve urban traffic management, reducing congestion, emissions, and commute times. The formal safety guarantees make deployment in safety-critical systems more responsible.

Potential Negative Impacts: Automated traffic control systems could be used for surveillance. The uncertainty quantification could be misused to justify risky decisions by cherry-picking confidence levels. We advocate for transparent deployment with human oversight and public accountability.

Limitations: Our experiments use simulated environments and historical data. Real-world deployment requires additional validation, hardware integration, and regulatory approval. The BY procedure’s conservatism may reduce anomaly detection power in low-dependence scenarios.

J. Extended Limitations and Future Work

J.1. Detailed Limitations

BY Conservatism. The Benjamini-Yekutieli procedure remains conservative under strong positive dependence. The correction factor $c_m = \sum_{i=1}^m 1/i \approx \ln(m) + 0.577$ can be substantial for large m (e.g., $c_m \approx 6.4$ for $m = 293$ nodes), reducing statistical power. While this ensures FDR control under arbitrary dependence, it may lead to missed detections in scenarios with weak or known dependence structure.

Block Bootstrap Validation. Block bootstrap (Section 4) verifies dependence exists but doesn’t formally justify BY (which requires no justification, holding under arbitrary dependence). It serves as a sanity check that BH’s independence assumptions are violated.

Constrained γ Stability. Unconstrained γ shows sign flips in 23% of training runs, occasionally inverting the intended attention behavior (attending more to uncertain neighbors). The Softplus constraint ($\gamma \geq 0$) eliminates this pathology.

Covariance Approximation. The spatial kernel $\rho_{ik} = \exp(-d_{ik}/\ell)$ is a simplification. Diagonal-only covariance reduces safety by 2.1% (Appendix C), suggesting the approximation is adequate but learned covariance could improve results.

Lyapunov Function Design. Designing appropriate Lyapunov functions requires domain expertise. Our neural Lyapunov approach learns the function from data, but the constraint structure (queue lengths, waiting times) must be specified by practitioners. Automated Lyapunov function discovery remains an open challenge.

Real-Time Deployment. While our 23ms inference latency is suitable for 15-minute control intervals, real-time deployment at finer granularities (e.g., second-level signal control) requires further optimization. Hardware acceleration (TensorRT, ONNX) and model compression could enable sub-millisecond inference.

Simulation-to-Real Gap. Our experiments use SUMO simulation and historical GPS data. Real-world deployment faces additional challenges: sensor noise, communication delays, actuator constraints, and edge cases not present in training data. Domain randomization and robust training could mitigate some of these issues.

Scale Limitations. The 4×4 SUMO network (16 intersections) is limited compared to real cities. Larger networks introduce: (1) partial observability requiring decentralized control, (2) coordination challenges across distant intersections, and (3) computational scaling concerns for real-time operation.

J.2. Future Work Directions

Adaptive BY with Dependence Estimation. Develop procedures that estimate the dependence structure online and adapt the FDR threshold accordingly. This could recover power lost to BY’s conservatism while maintaining finite-sample guarantees.

End-to-End Differentiable Conformal Calibration. Current conformal prediction is a post-hoc calibration step. Differentiable conformal training could enable joint optimization of prediction and calibration, potentially improving efficiency.

Multi-City Transfer Learning. Train on multiple cities and transfer to new cities with limited data. Graph structure provides a natural inductive bias; we hypothesize that attention patterns and uncertainty relationships transfer across similar urban topologies.

Real-World Pilot Deployment. Partner with municipal traffic authorities for pilot deployment. This requires: (1) integration with existing infrastructure (SCATS, SCOOT), (2) fail-safe mechanisms with human override, (3) A/B testing protocols, and (4) regulatory compliance.

Hierarchical Control. Extend to hierarchical architectures with: (1) intersection-level reactive control, (2) corridor-level coordination, and (3) city-level strategic planning. Different uncertainty quantification and safety guarantees may be appropriate at each level.